# CHAPTER 4

## Synthesis, application and optimization studies of polyaniline/activated carbon/copper cobaltite based composite material

### 4.1 Introduction:

The primary objective of the current study is to develop a ternary hybrid composite material that exhibits exceptional specific capacitance, specific energy-density, and specific power-density with enhanced cycle life. As discussed in chapter 2, composite materials generally demonstrate superior electrochemical performance compared to individual materials. In this chapter, a comparison of the electrochemical performances of pristine polyaniline (PANI) matrix, binary polyaniline-activated carbon (PANI/AC), binary polyaniline- copper cobaltite (PANI/CuCo), and ternary hybrid composite polyaniline/ activated carbon/ copper cobaltite (PANI/AC/CuCo) has been discussed.

For the synthesis of PANI, 9.40 g of aniline monomer along with 28.5 g of ammonium persulfate and 8.61 g of p-toluene sulfonic acid was taken. For the preparation of binary and ternary composite materials, 2.30 g of activated carbon and copper cobaltite each was used, ensuring a weight ratio of 4:1 for the binary composites (PANI: AC) and (PANI/CuCo) and 4:1:1 for the ternary composite (PANI/AC/CuCo). In the latter part of this chapter, optimization studies of the weight percentage of the ternary composite have been performed. Through these comparative and optimization studies, we aim to identify the composite material composition that yields the best specific capacitance and reasonably good specific energy density, specific power density, and cycle life.

**Part I: Electrochemical performance of pristine PANI, binary PANI/AC, binary PANI/CuCo, and ternary PANI/AC/CuCo materials**

### 4.2 Result and discussion

#### 4.2.1 X-ray diffraction

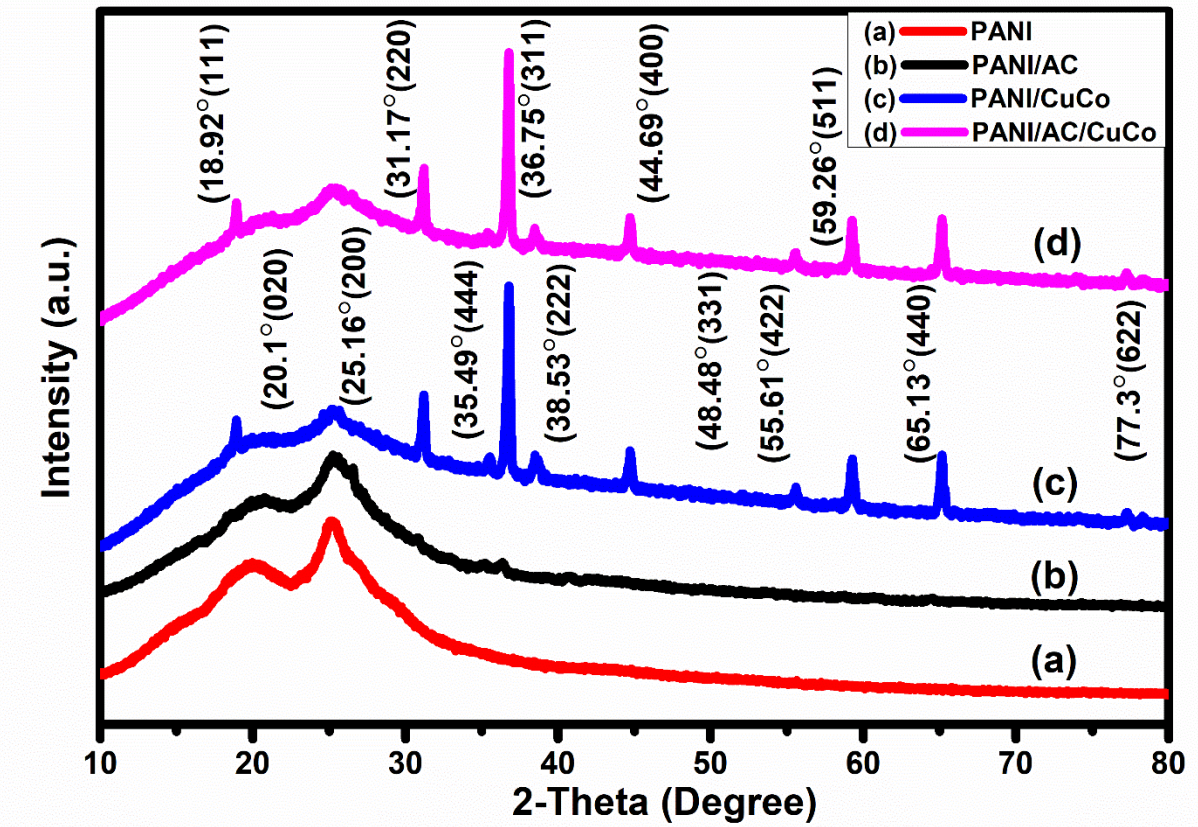


**Fig 4.1:** (A) XRD patterns of pristine PANI, binary PANI/AC, binary PANI/CuCo, and ternary PANI/AC/CuCo

The X-ray diffraction (XRD) spectra were employed to confirm the successful synthesis of the prepared materials. Figure 4.1 demonstrates the XRD patterns of pure polyaniline (PANI), binary polyaniline-activated carbon (PANI/AC), binary polyaniline-copper cobaltite (PANI/CuCo), and ternary polyaniline-activated carbon-copper cobaltite (PANI/AC/CuCo). The XRD peaks at 20.01° and 25.2° for pristine PANI confirm its successful synthesis. The XRD spectra of AC has been shown in fig. A1 (in appendix). The characteristic diffraction peak of AC merged to form a single peak at 25.39° in the case of binary PANI/AC. It is evident that PANI and AC show $\pi$-$\pi$* stacking interactions which enhances the electron transfer efficiency for the composite material [225]. The diffraction peaks of copper cobaltite (CuCo) were observed at 19.12° (111), 31.30° (220), 35.65° (444), 36.89° (311), 38.89° (222), 44.86° (400), 55.79° (422), 59.38° (511), 65.36° (440), and 77.41° (622), respectively (JCPDS 01-

1155) [226] (Fig. A1 (A) in appendix). Further, a crystalline size of 47.84 nm was obtained as calculated by Bragg's formula (eq. 3.5). The presence of diffraction peaks at 18.92° (111), 31.17° (220), 35.49° (444), 36.75° (311), 38.53° (222), 44.69° (400), 55.61° (422), 59.26° (511), 65.13° (440), and 77.30° (622) mark the successful incorporation of CuCo nanoparticles in PANI/AC to form PANI/AC/CuCo.

The binary and ternary composite materials displayed all the expected XRD peaks, although slight shifting in their positions was observed. It is noteworthy that the presence of CuCo particles resulted in weakening of characteristic peaks PANI in PANI/CuCo and PANI/AC/CuCo, consequently reducing their mass volume percentage [227].

### 4.2.2 FTIR

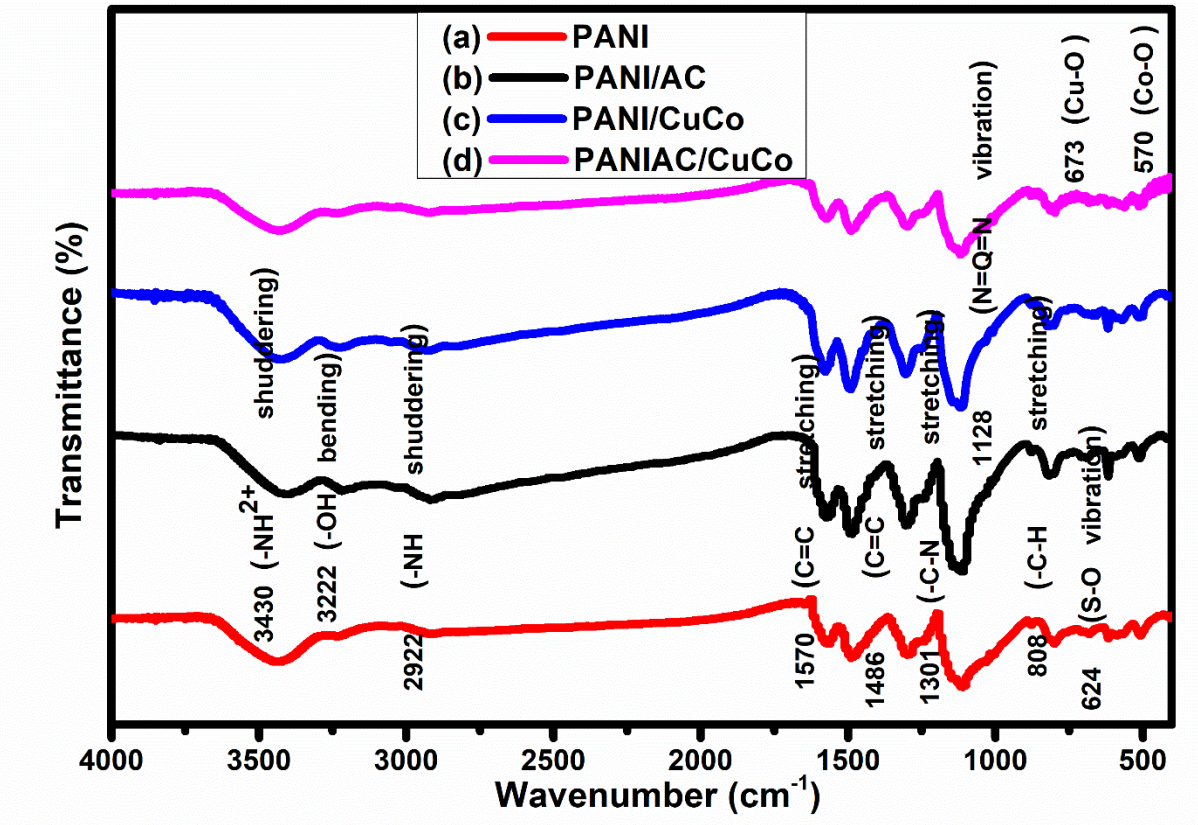


**Fig 4.2:** FTIR patterns of pristine PANI, binary PANI/AC, binary PANI/CuCo, and ternary PANI/AC/CuCo

The FTIR absorption spectra for prepared samples PANI, PANI/AC, PANI/CuCo, and PANI/AC/CuCo were recorded and presented in figure 4.2. For polyaniline (PANI), the humps at 3222 $cm^{-1}$ and 3428 $cm^{-1}$ were attributed to -OH and $-NH^{2+}$ bending, respectively [228,229]. The absorption band at 2922 $cm^{-1}$ conforms to -NH stretching. Also, the C=C stretching in the quinoid ring was marked by the absorption hump at 1570 $cm^{-1}$. The peak at 1486 $cm^{-1}$ was ascribed to C=C stretching benzoid rings, indicating the presence of conducting form of PANI. As commonly observed, the benzoid band at 1486 $cm^{-1}$ is more intense than that of the quinoid band at 1570 $cm^{-1}$ in PANI, which marks the higher presence of benzoid form. This higher intensity of benzoid form is also present in other binary and ternary composite materials. The -C-N shuddering in quinoid rings was associated with a peak at 1299 $cm^{-1}$, indicating the successful synthesis of protonated PANI. The hump at 1128 $cm^{-1}$ referred to p-substituted N=Q=N vibrations. This strong characteristic band is considered to behave as 'electron-like band' and is a measure of delocalization of electrons, and therefore indicates the conductivity of PANI [230]. The hump at 808 $cm^{-1}$ was attributed to -CH deformation indicating the presence of PTSA in PANI [231]. The presence of $-SO_3$ was confirmed by the appearance of band at 624 $cm^{-1}$. For AC, a strong stretching band was observed at 3430 $cm^{-1}$ exemplified O-H due to moisture content. The characteristic band for AC due to C-O stretching was also clearly visible at 1070 $cm^{-1}$ (Fig. A2 (A) in appendix). For PANI/AC composite, its formation is considered to arise from the $\pi$-$\pi$* interactions between AC particles and aniline monomer. Due to the effect of such interactions, the addition of PANI with carbon-based materials enhances the stability, functionality, and conductivity of PANI-based materials [232]. For PANI/CuCo, two additional absorption bands at 673 and 570 $cm^{-1}$ were present due to CuO and CoO functional groups from copper cobaltite. The strong characteristic peak of PANI is shifted to a slightly higher value in the composite materials, which may be due to protonated

state of PANI, and the extent of the shift depends on the amount of AC and CuCo used. All other corresponding bands could also be observed with slight shifting in the PANI/AC/CuCo ternary composite.

### 4.2.3 Morphological analysis

The surface morphology investigations of the prepared materials were performed with the help of a field emission scanning electron microscope (FESEM), as shown in figure 4.3. PANI exhibited rod-like morphology, which may be due to micelle formation. The AC exhibits its typical porous morphology ((Fig. A3 (A) in appendix)), and the CuCo nanoparticles show irregular morphology (Fig. A3 (B) in appendix). The binary composites PANI/AC and PANI/CuCo show somewhat interconnected structures that are not as rod-like as PANI.

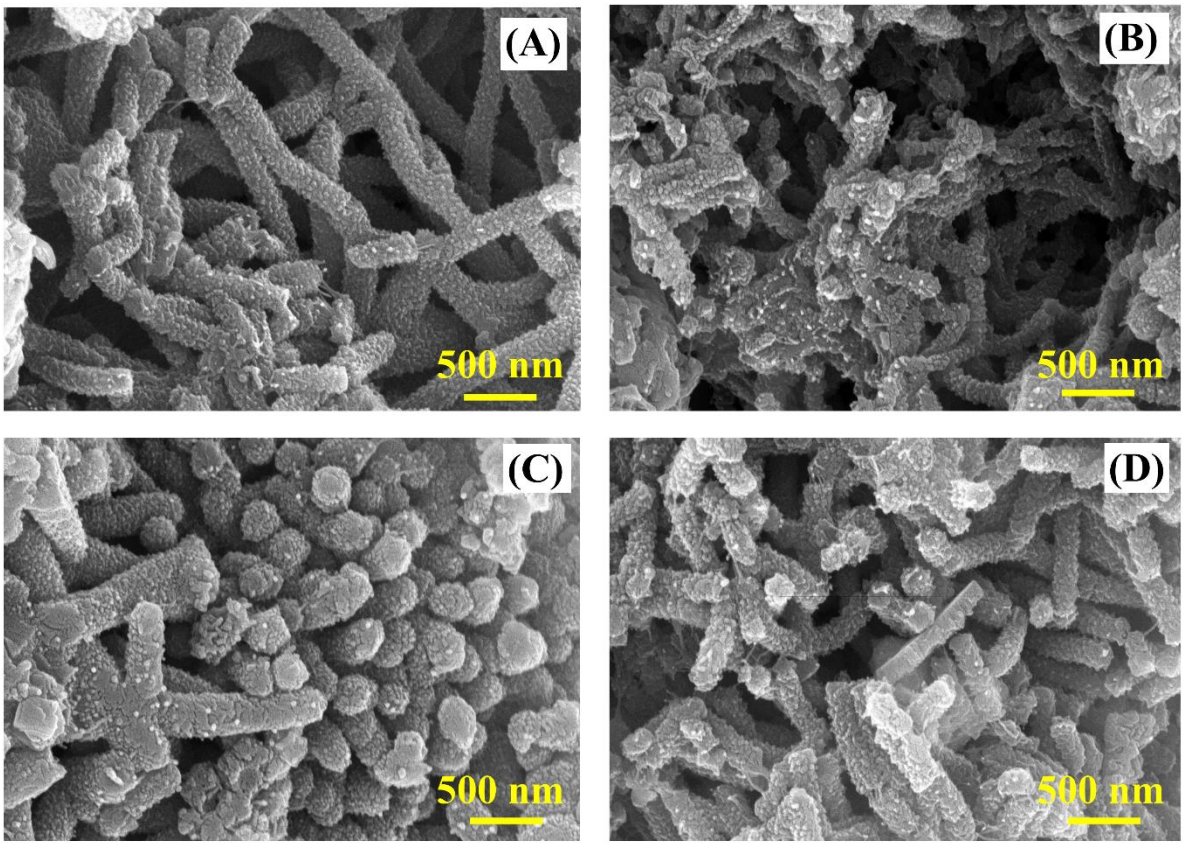


**Fig 4.3:** FESEM micrographs of (A) PANI, (B) PANI/AC, (C) PANI/CuCo, and (D) PANI/AC/CuCo

These rod-like structures, due to the presence of PANI, support electrical interactions throughout the material. The hydrophilic structure of -$SO_3H$ and lipophilic chain of $C_7H_8$ are the primary reasons behind amphophilic behavior of PTSA, which makes it a perfect structure-reforming material. When hydrophobic aniline comes in contact with -$SO_3H$ in PTSA, it forms an aniline-PTSA complex, which results in the formation of soft templates. In the case of binary and ternary composite materials, the addition of AC and CuCo alters the structures of micelles, as can be observed in the FESEM images when polymerization was started by adding APS, rod-shaped textures manifested according to the micelle formed [235]. The incorporation of PANI with AC and CuCo to form ternary composite PANI/AC/CuCo helps control the aggregation of CuCo in composite material. This type of morphology may enhance the effective liquid-solid interfacial area and support rapid electrolyte ion transportation during electrochemical characterizations [226].

### 4.2.4 EDX and elemental mapping:

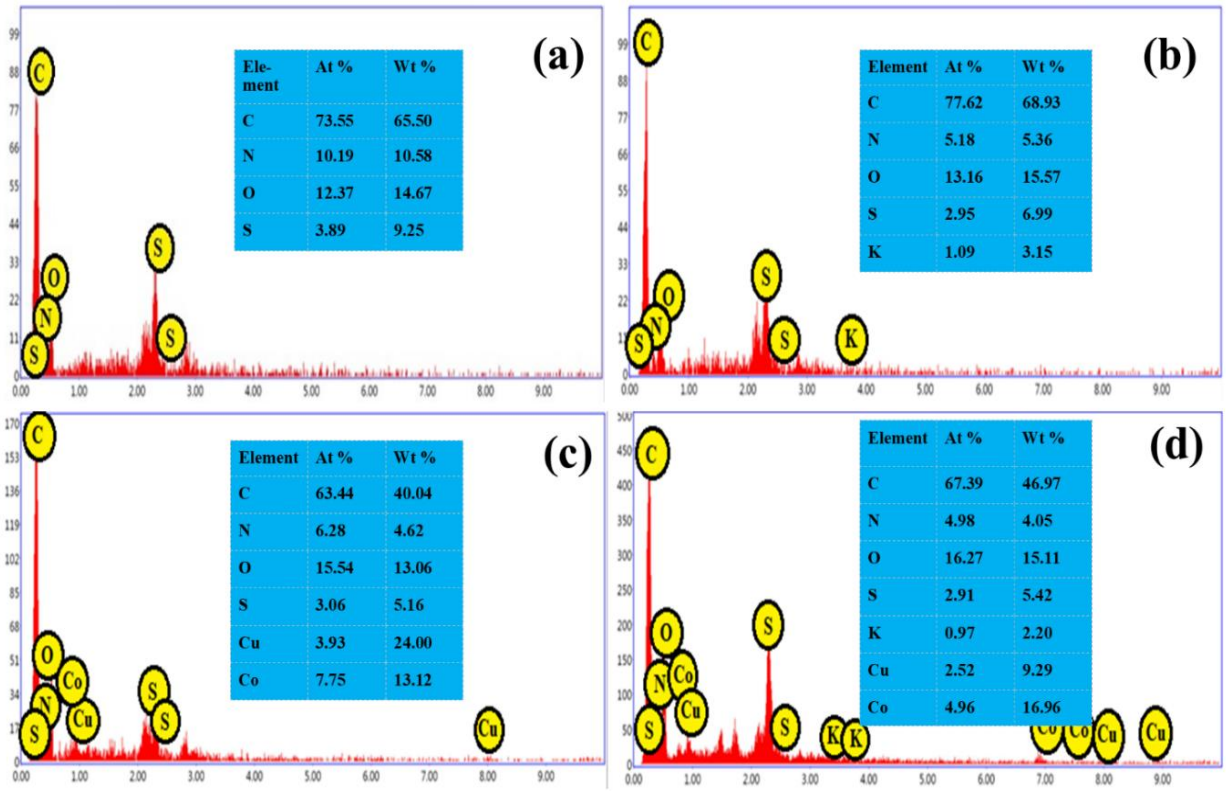

**Fig 4.4:** EDX analysis of (A) PANI, (B) PANI/AC, (C) PANI/CuCo, and (D) PANI/AC/CuCo

The details of elemental analysis of the prepared materials PANI, PANI/AC, PANI/CuCo, and PANI/AC/CuCo have been shown in figure 4.4, showing the presence of all the expected elements. The elemental analysis results indicate that C % has increased in the case of PANI/AC compared to PANI, which may be due to the incorporation of AC into PANI. Further, the C % decreased in the case of binary PANI/CuCo and ternary PANI/AC/CuCo composite materials owing to the presence of other elements. There is a significant reduction of N % in the case of PANI/AC as compared to PANI, which may be due to increased C and O % in the form of AC. The composition of S is minimum in the case of PANI, which may be due to extensive washing of the sample to remove excessive monomer and oxidant. Also, there is no significant change in the composition of O and S in binary and ternary composite materials compared to PANI. In the case of binary PANI/CuCo and ternary PANI/AC/CuCo, the Cu and Co atomic ratio is approximately 0.5, which is relatable from the formula $CuCo_2O_4$. The presence of K is also visible which is due to the activation of AC with KOH.

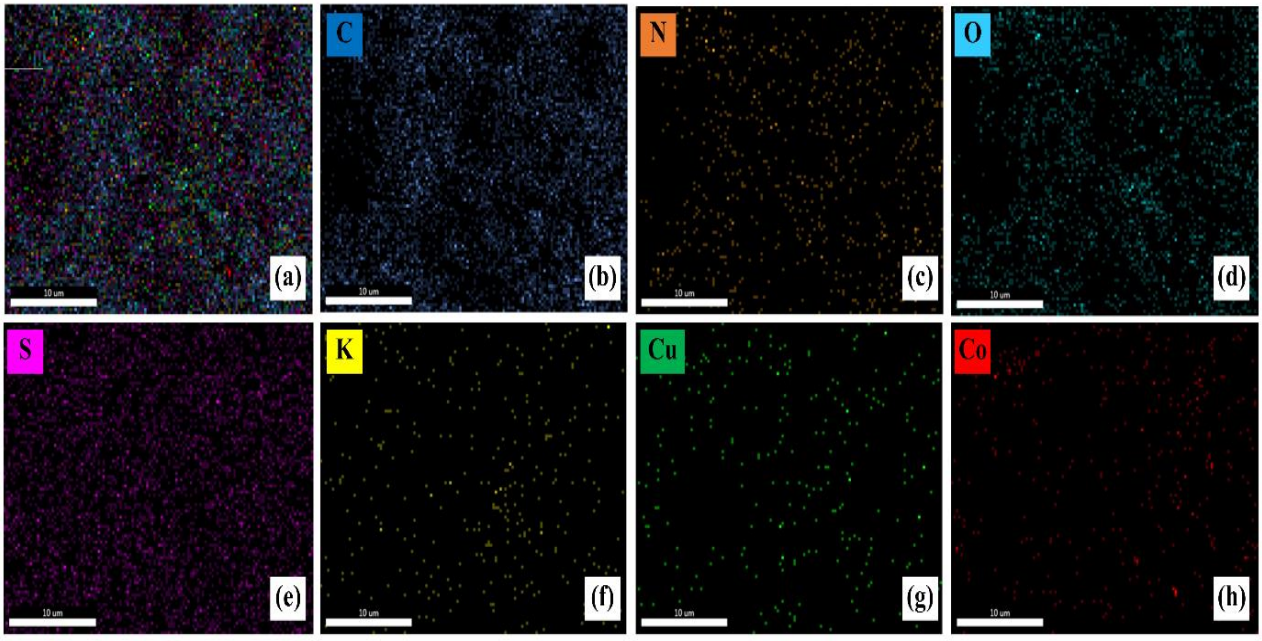


**Fig 4.5:** Elemental mapping of ternary composite material PANI/AC/CuCo.

The elemental mapping (combined and individual) of the ternary composite material PANI/AC/CuCo has been demonstrated in figure 4.5. A uniform mapping pattern can be observed in figure 4.5 (a). Also, the mapping patterns of C, N, O, and S demonstrate their higher concentration as compared to that of K, Cu, and Co in the ternary composite PANI/AC/CuCo in figure 4.5 (b) to (h).

### 4.2.5 X-ray photoelectron spectroscopy

X-ray photoelectron spectroscopy was employed to verify the surface composition of prepared materials. The survey scan (Figure 4.6) exhibited the presence of C, N, O, and S in all the samples. The intensity of C1 s peaks is much higher than that of O1 s in the survey scans, which indicates that oxygen-bearing functional groups are relatively lesser. These observations are in good agreement with the EDX results. The high-resolution fitted spectrum of PANI/AC (Fig. A4 in appendix) demonstrated four different peaks at 284.51 eV, 285.51 eV, 286.92 eV, and 290.71, respectively. These peaks can be attributed to (C-C) & (C=C), (C-O), (C=O) groups and $\pi$-$\pi^*$ "shake-up" satellite band due to the presence of AC, respectively [236]. This $\pi$-$\pi$ interaction might facilitate the charge transfer process, thereby creating an efficient conducting network that is advantageous for the ion diffusion process and quick redox reaction, leading to a high capacitance [237,238]. Further, the presence of Cu and Co was also evident in the case of binary PANI/CuCo and ternary PANI/AC/CuCo.

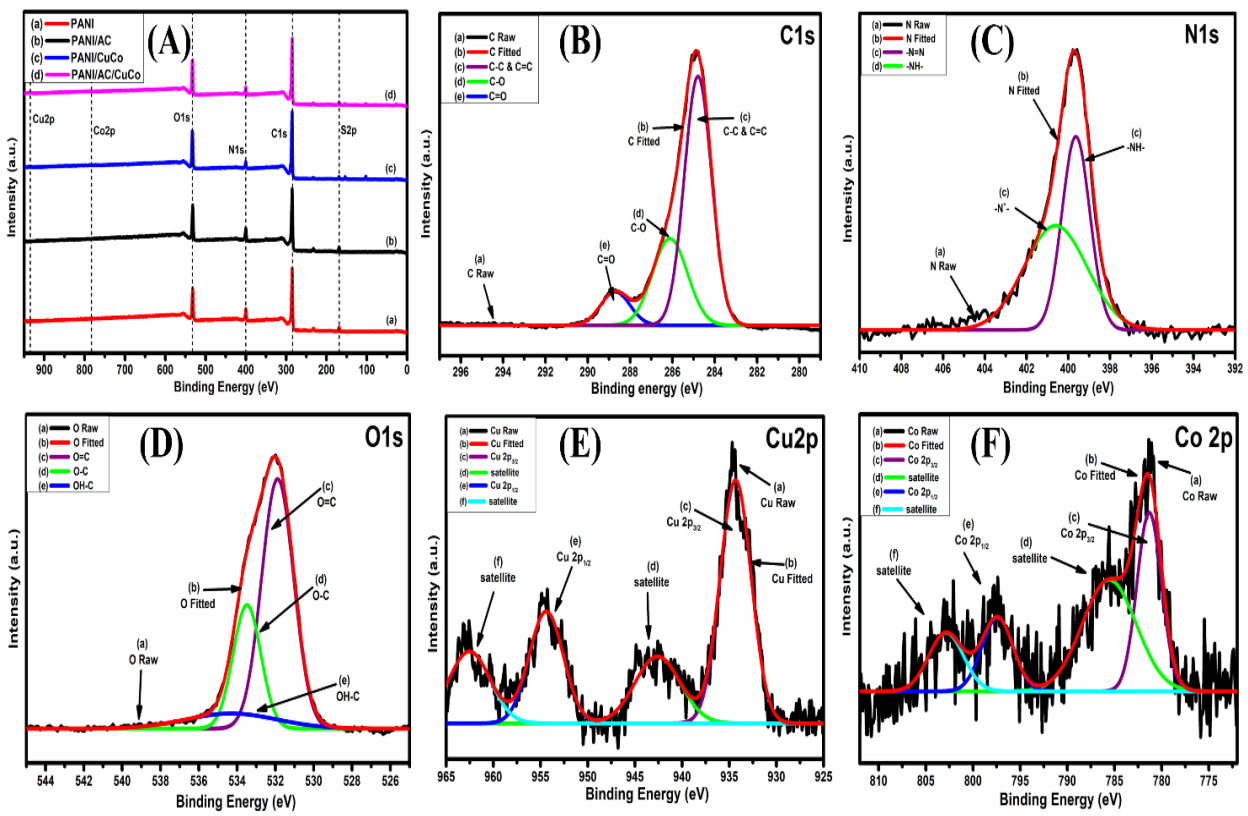


**Fig 4.6:** (A) XPS survey scan of PANI, PANI/AC, PANI/CoF, PANI/AC/CoF, (B) to (F) high-resolution spectra for C1s, N1s, O1s, Cu2p and Co2p, respectively.

The high-resolution spectrum of C1s in the case of ternary PANI/AC/CuCo (Figure 4.6 (B)) demonstrated three specific peaks. The peaks at 284.78, 286.10, and 288.72 eV were attributed to (C-C) & (C=C), (C-O) in alkoxy/epoxy, (C=O) in carboxylic groups, respectively. The high-resolution spectrum of N1s (Figure 4.6 (C)) manifested two peaks, at 399.6 and 400.6 eV, which were due to benzoid amine (-NH-) and N cationic radical. These two are the fingerprint-binding energies of polyaniline, confirming the presence of conducting form of polyaniline [239]. The high-resolution spectra of O1s (Figure 4.6 (D)) were deconvoluted into three peaks at 531.86, 533.48, and 534.4 eV. These peaks were attributed to double-bond aromatic carbon (C=O), single-bond oxygen to carbon (C-O), and single-bond carbon to a hydroxyl group (C-OH), respectively [240,241].

The high-resolution XPS spectra of Cu (Figure 4.6 (E)) in ternary PANI/AC/CuCo deconvoluted into two primary and two satellite peaks. The peaks at 934.31 eV were due to Cu $2p_{3/2,}$ and that at 942.6 eV was assigned as its satellite peak. Similarly, the peak at 954.44 eV confirmed the presence of Cu $2p_{1/2,}$ with its satellite peak at 962.51 eV [242,243]. Additionally, the two sharp peaks at binding energies 781.29 and 797.49 eV (Figure 4.6 (F)) were present due to Co $2p_{3/2}$ and Co $2p_{1/2}$ with respective satellite peaks at 785.6 and 802.8 eV [240].

### 4.2.6 Transmission electron microscopy

Transmission electron microscopy was performed for the prepared ternary composite PANI/AC/CuCo, as shown in figure 4.7 below. The presence of all three constituents was confirmed with the help of TEM results. Porous-activated carbon could be observed clearly in the low-resolution micrograph with polyaniline nanorods in the background. In the high-resolution micrograph, the copper cobaltite nanoparticles could be seen sitting inside the pores of activated carbon. In general, metal oxide possess lower surface area than activated carbon. In the case of composite materials, due to higher density of metal oxides, they bear a tendency of getting settled inside the porous structure of activated carbon. The synergistic effect is achieved by virtue of interconnected PANI networks and CuCo embedded into AC and hence effects of all the materials involved comes into play contributing together towards better performance of the material. Also, this scattering of particles helps in maintaining the stability of metal oxides and regulating their morphology during abrupt volume change which in turn otherwise lowers the capacitance retention of composite material as discussed in chapter 2.

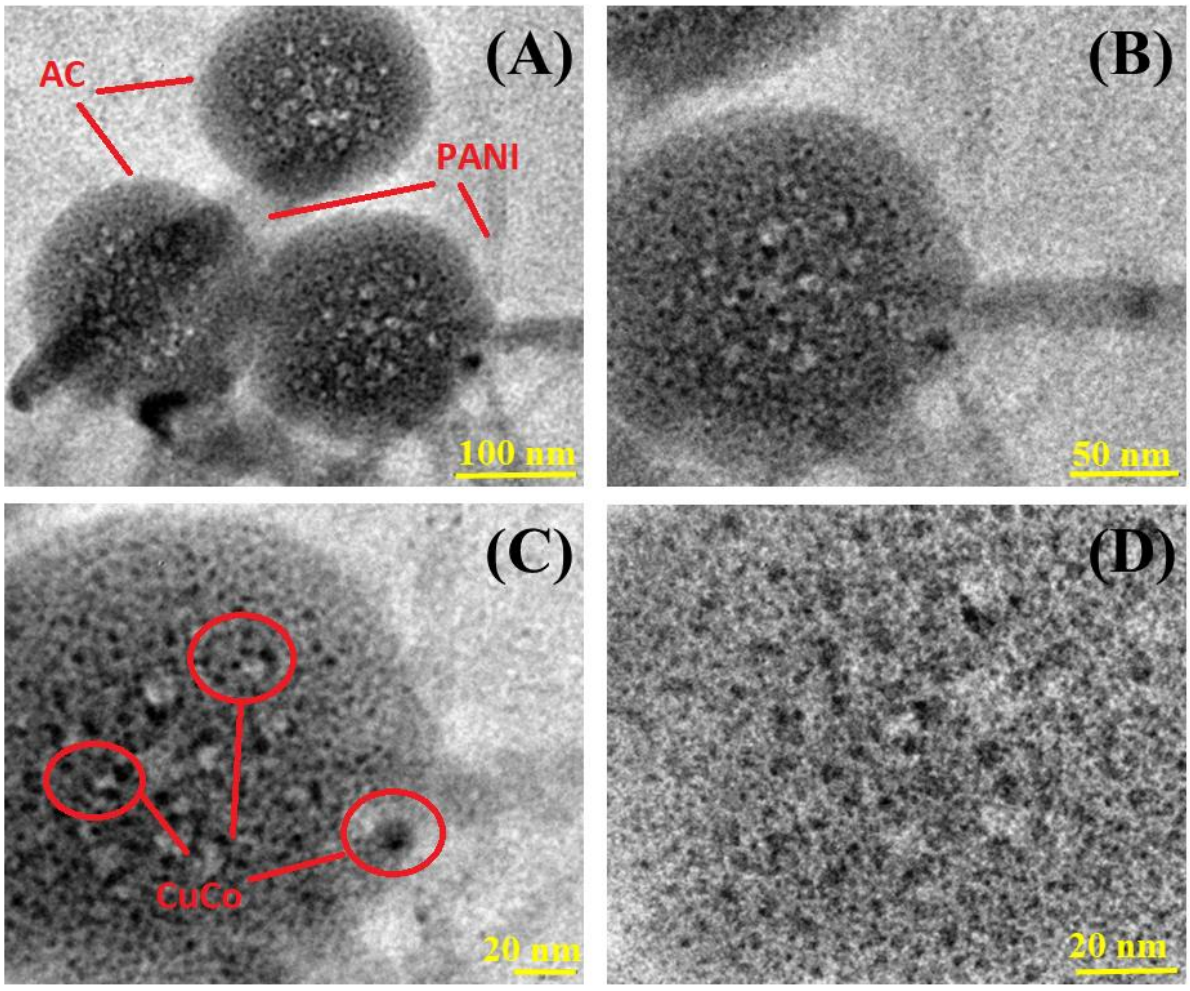


**Fig 4.7:** (A) to (D) TEM micrographs of ternary composite material PANI/AC/CuCo at different resolutions

### 4.3 Electrochemical characterizations:

Cyclic voltammetry of the prepared electrodes was performed at a voltametric scan rate of 1 mV/s. The stable potential window for the electrodes was found to be between -0.2 V to 1.0 V. Therefore; all the electrochemical characterizations were performed in the same potential range. The potential window has been selected considering the fact that both the electrode active material and electrolyte must not degrade in that potential range. The selected potential is the stability window for these prepared materials. Figure 4.8 shows the CV diagrams for all the prepared materials at a scan rate of 1 mV/s.

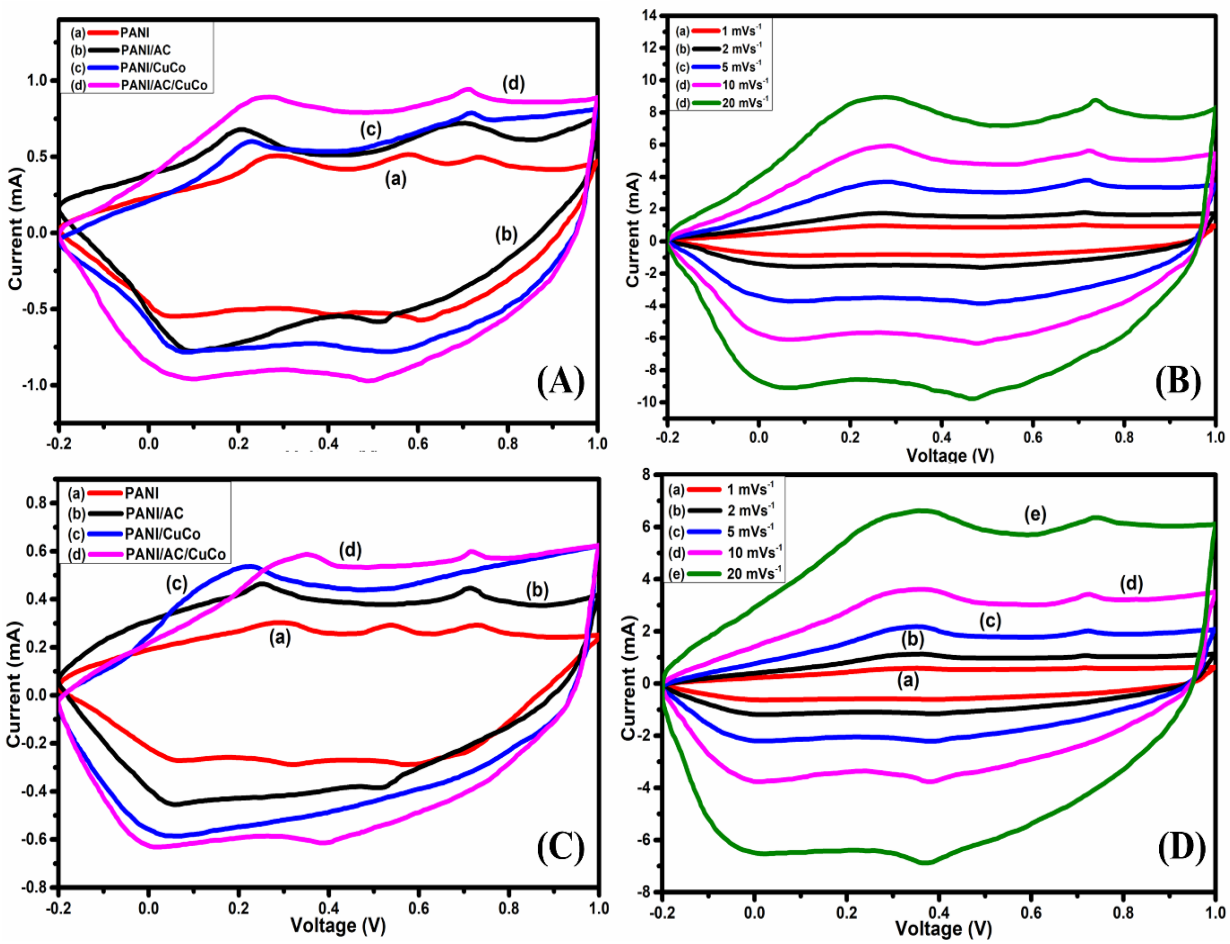


**Fig 4.8:** (A) 3E CV of prepared materials, (B) 3E CV of ternary PANI/AC/CuCo at varying scan rates, (C) 2E CV of prepared materials, (D) 2E CV of ternary PANI/AC/CuCo at varying scan rates from 1-20 $mVs^{-1}$

Pristine PANI exhibited three pairs of redox peaks in figure 4.8 (A). The oxidation peaks were at 0.29, 0.57, and 0.72 V. The peak at 0.29 is attributed to the redox change of PANI from leucoemeraldine to emeraldine form, whereas the peak at 0.57 signifies degraded benzoquinone/ hydroquinone. The hump at 0.72 refers to the switchover from emeraldine to pernigraniline form of PANI [244]. Different redox transition states of PANI have been presented in fig. A5 (in appendix).

On the other hand, the reduction peaks of PANI could be seen at 0.61, 0.40, and 0.04 V. For PANI/CuCo, and ternary PANI/AC/CuCo composites. In the binary composite PANI/AC, the

two pairs of redox peaks were present at 0.20/0.69 and 0.52/0.08 for the forward and backward sweep, respectively. This shifting of peaks may be due to strong interactions between PANI and AC. For PANI/CuCo, the peaks at 0.22 V and 0.71 V were attributed to $Co^{3+}/ Co^{4+}$ and $Cu^{2+}/ Cu^{3+}$ transitions, respectively, in the presence of PANI. The redox reaction mechanism of $CuCo_2O_4$ has been presented in appendix (eq. A). In the case of ternary composite PANI/AC/CuCo, the peaks in the forward scan were located at 0.26/ 0.71 V, whereas those in the reverse scan were at 0.49/0.08 V, respectively. The oxidation peak at 0.57 V could not be seen in the case of binary PANI/AC, PANI/CuCo, and ternary PANI/AC/CuCo, which may be due to the involvement of AC and CuCo particles. This involvement is because CuCo particles possess high density, and AC are known to have high surface area; therefore, the metal oxides have been dispersed into AC sites swaddled by PANI rods, as evident from the morphological studies discussed earlier. These interconnected structures were responsible for the highest voltammetric area in the case of the ternary composite PANI/AC/CuCo. The porous structure of AC creates channels for ion transport, thus, the PANI and CuCo deep inside the active material can easily participate in the redox reactions. The specific capacitance values for PANI, PANI/AC, PANI/CuCo, and PANI/AC/CuCo at 1 $mVs^{-1}$ were 389.6, 522.2, 551.6, and 613.5 $Fg^{-1}$, respectively. This higher specific capacitance of ternary PANI/AC/CuCo may be due to synergistic effects between individual components of the composite. The ternary composite was also tested under varying voltammetric scan rates of 2, 5, 10, and 20 $mVs^{-1}$ (Figure 4.8 (B)). The specific capacitance values for ternary PANI/AC/CuCo at these scan rates were calculated as 543.7, 483.2, 415.8, and 325.9 $Fg^{-1}$. The peak current responses increase with the increase in scan rate implying a rapid charge propagation. The voltammetric area under the successive curves increases with the scan rate [245], conforming to the highly capacitive nature of the prepared ternary material. The peaks were shifted slightly to the right side for the forward sweep. On the other hand, for the reverse sweep, the peaks moved somewhat to the left side.

This shifting may be due to strong electric polarization and possible kinetic irreversibility of electrolyte ions at the electrode surface at high scan rates [226].

The prepared electrodes were also evaluated under a two-electrode symmetric configuration at 1 $mVs^{-1}$ scan rate (Figure 4.8 (C)). The ternary composite PANI/AC/CuCo demonstrated the highest voltammetric area and highest value of peak current. The composite material's dual nature (EDLC and pseudocapacitance) was the reason behind the extraordinary performance of the ternary composite. Moreover, with the rise in scan rates from 2, 5, 10, and 20 $mVs^{-1}$, the voltammetric area under the curves increases due to a rise in capacitive current with scan rates (Figure 4.8 (D)). On the other hand, specific capacitance value declines rapidly with a rise in scan rates as the electrolyte ions do not get a plentiful amount of time to reach the pores and interact with the electroactive species at the active sites. For this reason, the prepared material could not respond to the reversible reduction-oxidation reactions at higher scan rates compared to lower scan rates. The galvanostatic charge-discharge tests were conducted for the synthesized electrodes under a two-electrode symmetric configuration. The charge-discharge plot at 1 $Ag^{-1}$ current density is shown in figure 4.9 (A). The ternary composite PANI/AC/CuCo exhibited the highest discharging time corresponding to its highest discharging time. This high performance may be attributed to improved electron and ion transport brought by incorporating PANI chains into AC, which provides a network and interconnecting pores. The binary PANI/CuCo and PANI/AC demonstrated less discharge time, followed by pristine PANI-based electrodes. The synthesized materials showed somewhat triangular behavior on the charge-discharge curve with minor plateaus. These plateaus exemplify the dual behavior (EDLC and pseudocapacitive). The ternary composite PANI/AC/CuCo was evaluated for GCD under varying current densities of 2, 5, 10, and 20 $Ag^{-1,}$ as shown in figure 4.9 (B). As the current density rises, the charging-discharging times decline, leading to shrinking specific capacitance values. This reduction in electrochemical performance may be due to the limited transportation

of electrolyte ions, thereby leaving certain packets of the electrode material unreachable under high current densities. The highly linear and symmetric GCD profiles at all the different current densities imply excellent reversibility and good rate capability of the electrodes [246].

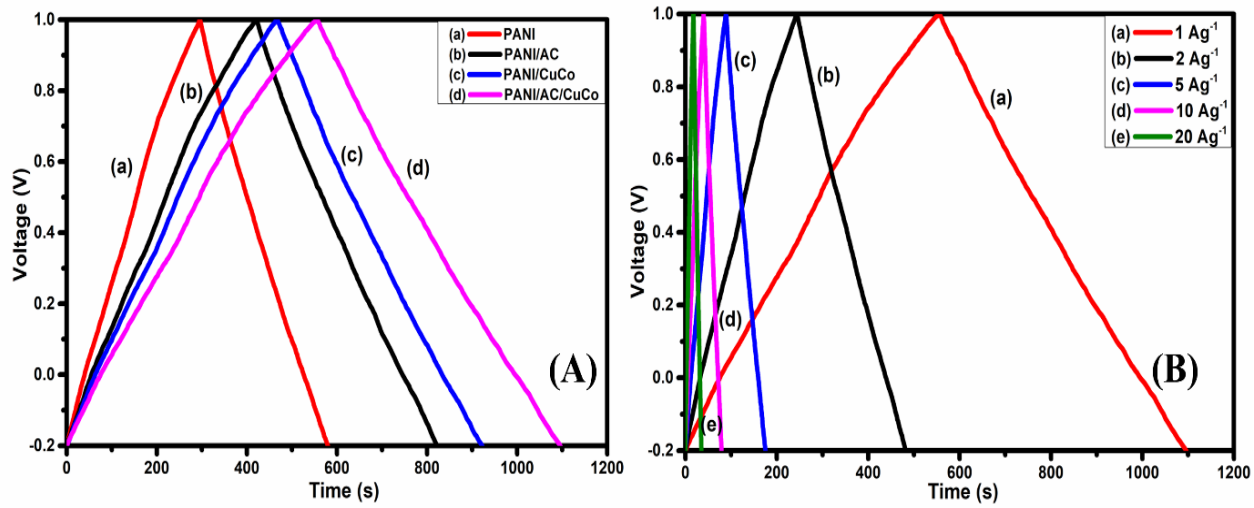


**Fig 4.9:** GCD characteristics of (A) PANI, PANI/AC, PANI/CuCo, and PANI/AC/CuCo at 1 A/g, (B) ternary PANI/AC/CuCo at varying current density from 1-20 $Ag^{-1}$.

Figure 4.10 (A) demonstrates the synthesized materials' Ragone plot (specific energy density vs. specific power density). The ternary composite PANI/AC/CuCo manifested the highest specific energy density against binary PANI/AC, PANI/CuCo, and pure PANI at almost the same specific power density, which attributes to the ternary composite showing maximum charge storage capacity than others. Moreover, at higher current densities, the specific energy density showed a negative trend with a rise in specific power density. Figure 4.10 (B) demonstrates the decline in measured values of 3- E specific capacitance as a function of scan rate.

The peak specific energy density for the ternary composite PANI/AC/CuCo was 44.1 $Whkg^{-1}$ and 301.0 $Wkg^{-1}$ of specific power density. The corresponding ternary system exhibited an utmost specific power density of 5997.1 W $kg^{-1}$ and a specific energy density of 27.5 $Whkg^{-1}$

at 20 A/g. The presence of AC (EDLC) and PANI/ CuCo (pseudocapacitive) helps uplift the ternary composite's specific energy density without much compromising its power density.

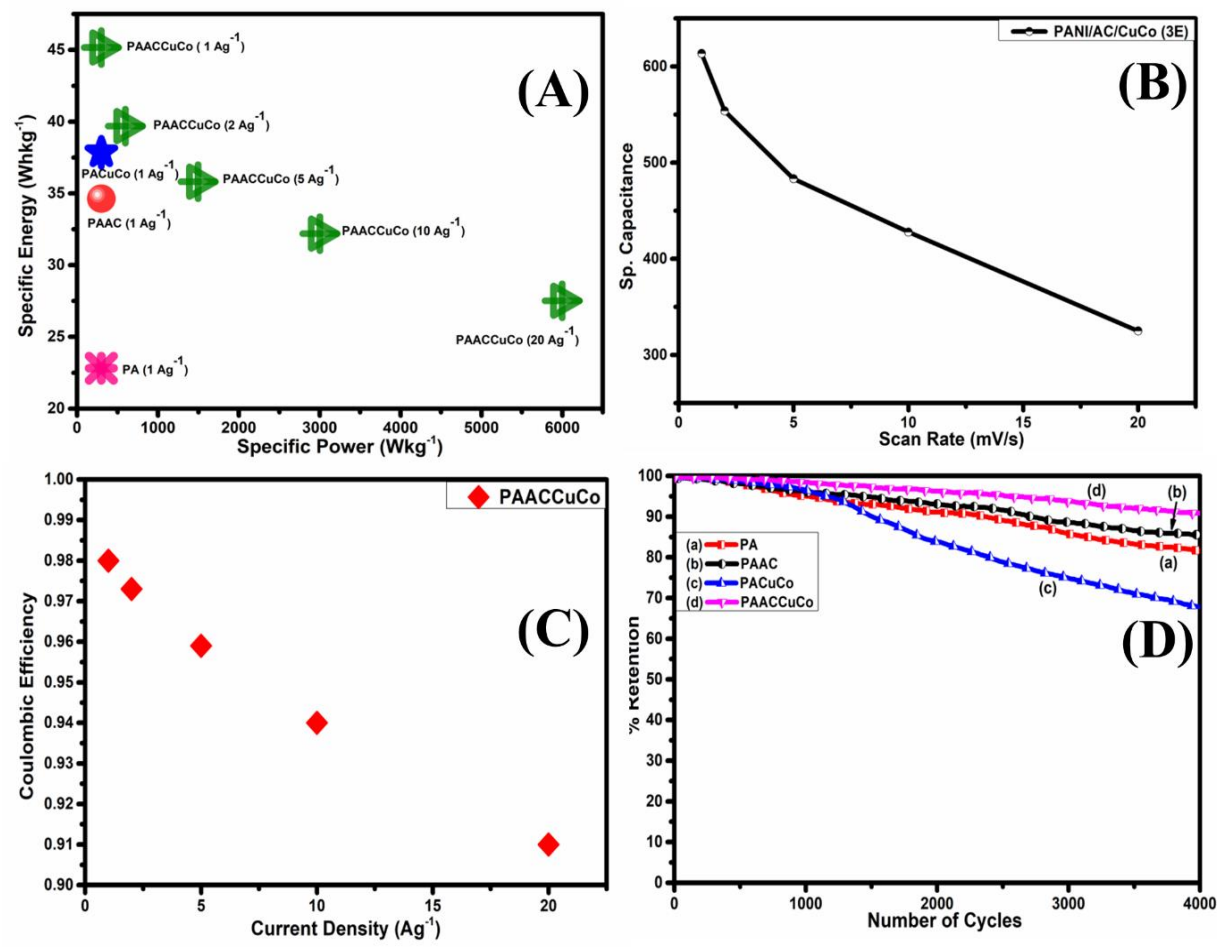


**Fig 4.10:** (A) Ragone plot for the prepared samples, (B) 3E specific capacitance values at different values of voltammetric scan rates, (c) current density vs. coulombic efficiency, (D) Capacitance retention curve

The coulombic efficiency is a measure to know about the charge transfer capability of a material and is defined as the ratio of charging time to the discharging time of the material as indicated by GCD plots (Figure 4.10 (C)), depicts the variation of coulombic efficiency with current density. It was observed that the coulombic efficiency declines as current density rises, which could be due to the elevated irreversibility of the material at a higher current density.

The ternary composite PANI/AC/CuCo showed exceptional coulombic efficiency of 92.8 %, even at 20 A/g.

The charge retention tests for the 2E symmetric system were also carried out to investigate the cyclic ability of the fabricated electrodes at a scan rate of 100 mV/s for 4000 cycles. The ternary composite PANI/AC/CuCo resulted in 90.76 % (Figure 4.10 (D)) capacitance retention, much higher than binary PANI/CuCo, PANI/AC, and pristine PANI samples. It is perceptible that pure PANI and CuCo display precipitous volume expansion and contraction, which restrict their cycling ability. The addition of AC supports the overall structure, enhancing the cyclic stability and addressing the uneven expansion-contraction within the material. Table 4.1 shows the different values of specific capacitance, specific energy-density, and specific power-density for different materials.

**Table 4.1:** The values of specific capacitance ($C_{SP}$), specific energy-density ($E_{SP}$), and specific power-density ($P_{SP}$) for various prepared samples.

| **Material** | **Scan Rate (mV/s)** | **$C_{SP}$ (CV 3-E)** | **Current Density (A/g)** | **Esp (Wh/kg)** | **Psp (W/kg)** |
|---|---|---|---|---|---|
| PANI | 1 | 389.6 | 1 | 22.8 | 299.9 |
| PANI/AC | 1 | 522.2 | 1 | 34.6 | 300.0 |
| PANI/CuCo | 1 | 551.6 | 1 | 37.8 | 298.9 |
| PANI/AC/CuCo | 1 | 613.5 | 1 | 44.1 | 301.0 |
| PANI/AC/CuCo | 2 | 543.7 | 2 | 39.6 | 597.6 |
| PANI/AC/CuCo | 5 | 483.2 | 5 | 35.8 | 1502.5 |
| PANI/AC/CuCo | 10 | 415.8 | 10 | 32.1 | 3002.3 |
| PANI/AC/CuCo | 20 | 325.9 | 20 | 27.5 | 5997.1 |

To study the impedance characteristics of the fabricated electrodes, EIS was performed in the 0.1 to 100000 Hz frequency regime in the form of Nyquist plots in figure 4.11 (A). In the high-frequency zone, these plots show the formation of a depressed semi-circle. These semi-circles are generally attributed to the presence of capacitance and electrode-electrolyte interfacial resistance parallel to each other. The intercept of the semi-circle in a high-frequency regime corresponds to the equivalent series resistance (ESR). The components contributing to ESR are inherent resistance of the active material, active material/ current collector contact resistance, and electrolyte resistance. The diameter of the depressed semi-circle reflects the value of charge transfer resistance (Rct), which involves the diffusion of ions in the electrolyte. The ternary PANI/AC/CuCo-based electrode manifested astonishingly low ESR and Rct values of 1.49 Ω and 5.6 Ω, respectively. The electrodes with binary composites PANI/CuCo and PANI/AC demonstrated slightly higher values of ESR/ Rct pairs at 2.5/5.01 Ω and 1.5/7.2 Ω. The electrode with pristine PANI exhibited ESR of 1.5 Ω and 7.6 Ω, respectively.

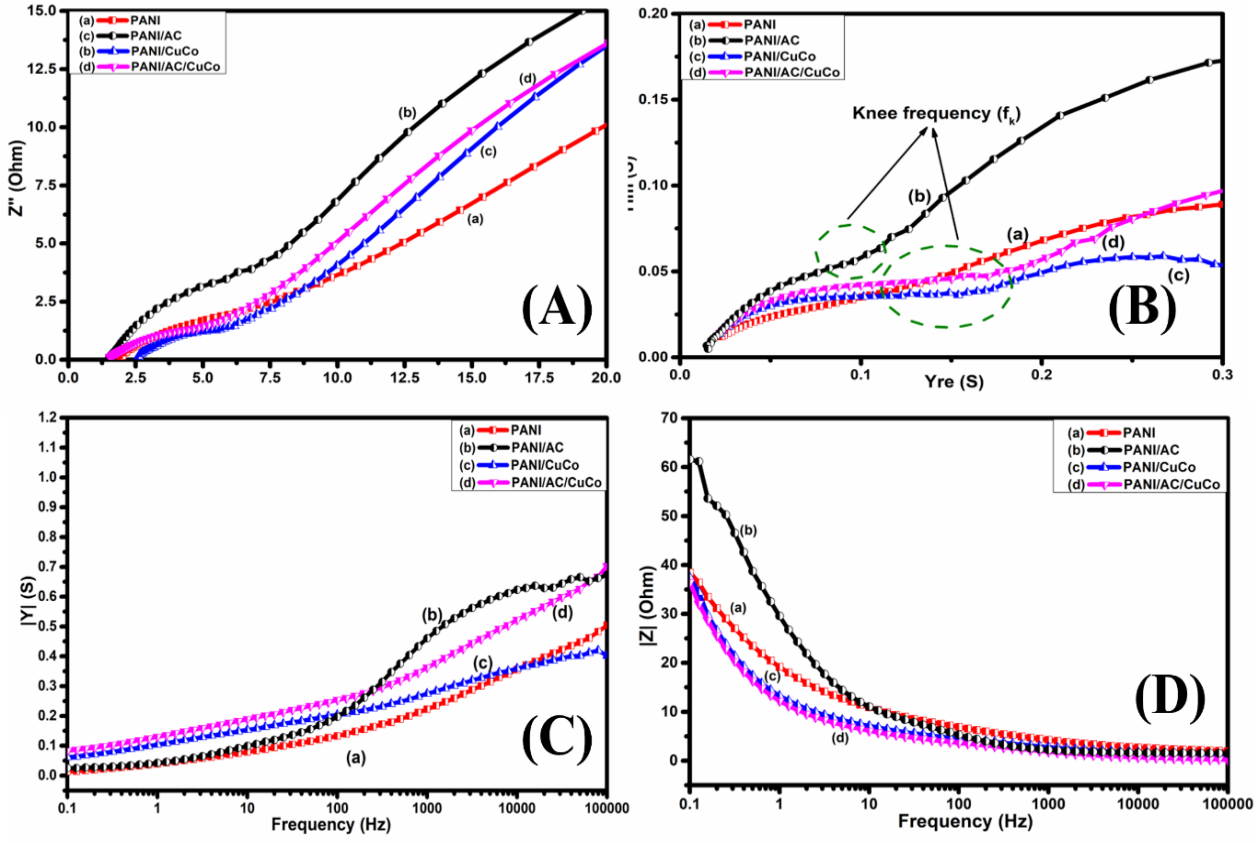


**Fig 4.11:** (A) Electrochemical impedance spectra (EIS) in the complex plane (B) Admittance plots in the complex plane. (C) normalized impedance |Z| vs. frequency, and (D) normalized admittance vs. frequency

Moreover, the slope of the Nyquist curve in the low-frequency region was assigned to the Warburg impedance, which is linked to the ionic diffusion process. This slope approaches infinity or is approximately parallel to the imaginary Z-axis for an ideal electrode comprising an ideal coating of the active material. The electrode with ternary PANI/AC/CuCo showed reasonably better performance as compared to others. These exceptionally lower values of the resistances could be the reason behind the linear characteristics of the charge-discharge curves and the high capacitance retention capability of the ternary composite PANI/AC/CuCo. The impedance spectra results conform to the low resistances furnished by the different components of the electrode, such as substrate, current collector, current collector/ active material, and the

electrolyte. The frequency response analysis of the prepared electrodes was extended to the study of admittance (Y'' vs. Y'), |Y| / |Z|, and |C| vs. frequency studies. Figure 4.11 (B) depicts the change of real (Y') vs. the imaginary (Y'') admittance for the fabricated electrodes of different materials. The admittance plots are used to calculate response time ($t_r$) and knee frequency ($f_k$).

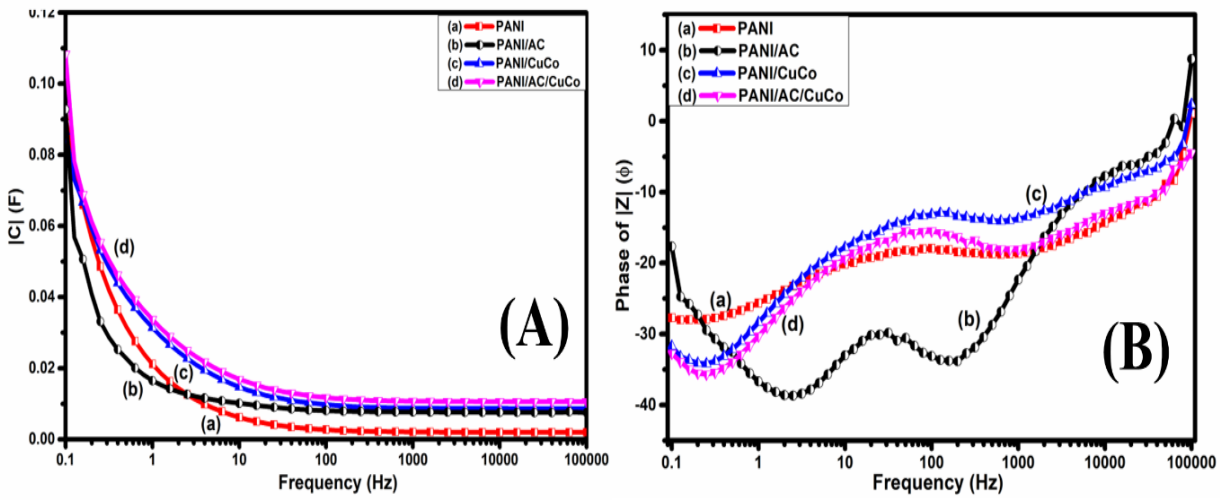


**Fig 4.12:** (A) normalized capacitance |C| vs. frequency, and (B) phase of |Z| (ϕ) vs. frequency

The frequency at which the stored charges can be fully utilized is called knee frequency. The $f_k$ corresponding to ternary composite PANI/AC/CuCo, binary PANI/CuCo, binary PANI/AC, and PANI was calculated to be 0.019, 0.031, 0.050, and 0.10 Hz, respectively, and the corresponding response times were found to be 50.11, 31.66, 19.95 and 10 s respectively. The materials exhibited quick response times, with ternary PANI/AC/CuCo being the most sluggish comparatively. This sluggish nature results from a large number of redox reactions in the background, which compete with each other over time. Figure 4.11 (C) manifests the change of admittance |Y| and frequency. It could be observed that |Y| increases with the rise in frequency for all the fabricated electrodes because, with an increase in frequency, the ions vibrate more; thus, their penetrating power gets elevated. The value of total admittance |Y| was highest for ternary PANI/AC/CuCo in both the low and high-frequency zone. Figure 4.11 (D)

shows the change in total impedance |Z| with frequency that declines as frequency [247]. For ternary PANI/AC/CuCo, the total impedance is lowest in both the high and low-frequency regimes, confirming the results from the Nyquist plots. Figure 4.12 (A) depicts the trend of total capacitance |C| with frequency. It was observed that the capacitance declines with increasing frequency values because, at low frequencies, the redox reactions occur better owing to lesser vibrations of ions present. It was clear that the ternary composite PANI/AC/CuCo demonstrated the highest total capacitance |C| in low and high-frequency regimes. These results were in good agreement with that of the EIS analysis. Figure. 4.12 (B) manifests the variation of the phase of Z ($\phi$) with frequency. In the case of PANI, the phase angle is around 28°, representing its pseudocapacitive nature. In PANI/AC, the increase in phase angle to 39° indicated that some EDLC behavior is introduced due to the presence of AC. The sample PANI/CuCo indicates a sharp change in phase angle to 34°, which could be due to the larger crystallite size of CuCo covering the active pores of PANI and inhibiting the desired redox transitions from occurring (making the system show EDLC nature). In the case of ternary PANI/ACCuCo, the addition of AC would have acted as a substrate for PANI and CuCo, providing enough support for the redox transitions to take place (decrease in phase angle to 36 ° due to both EDLC and pseudocapacitive nature of prepared composite).

### 4.4. Conclusion

A novel low-cost ternary composite material polyaniline-activated carbon-copper cobaltite (PANI/AC/CuCo) was synthesized and characterized with the help of XRD, FTIR, FESEM, EDX, TEM, and XPS. The inherently EDLC behavior of activated carbon and pseudocapacitive behavior of polyaniline and copper cobaltite together rendered excellent electrochemical activity of the ternary composite. Therefore, the composite has been synthesized to take advantage of the individual components. The specific capacitance values of the ternary composite PANI/AC/CuCo at 1 $mVs^{-1}$ was 613.5 $Fg^{-1}$. The symmetric device

based on PANI/AC/CuCo demonstrated a high specific energy-density of 44.1 Wh/kg and a maximum specific power density of 5997.1 W/kg. The ternary composite PANI/AC/CuCo resulted in 90.76 % of capacitance retention after 4000 cycles. This robust stability may be due to activated carbon, which maintains the inherency of polyaniline and copper cobaltite. EDLC behavior of activated carbon and the presence of redox-active sites in polyaniline and copper cobaltite (pseudocapacitance) are responsible for the outstanding electrochemical property of the ternary composite PANI/AC/CuCo. The lowest charge transfer resistance is shown by the ternary composite PANI/AC/CuCo, which is also the system with the highest cycle life. The ternary composite's beneficial outcomes make it a good contender for supercapacitor applications.

**Part II: Optimization of ternary composite material PANI/AC/CuCo**

In this work, ternary composite material PANI/AC/CuCo was optimized by varying the weight percentage of AC and CuCo and taking a fixed weight percentage of PANI using the response surface methodology for supercapacitor application.

## 4.5 Central Composite Design

The electrochemical property of the prepared ternary composite material electrode is greatly influenced by the amount of AC and CuCo used. It is essential to understand how their weight percent parameter affects the electrochemical behavior in order to improve the specific capacitance value. Hence, optimization of weight percentage of AC and CuCo is important. Response Surface Methodology (RSM) is amongst the most effective and extensively used techniques for optimization. The RSM’s central composite design was utilized to optimize the weight percentage of AC (A) and weight percentage of CuCo (B) in ternary composite with fixed weight percentage of PANI for electrochemical supercapacitor performance. This method offers a simple way to assess the interactions between various variables and only calls for a

limited number of operations to optimize the response variable. Table 4.2 displays the experimental factor levels that were employed for optimization and the variables. The outcomes of basic experiments with 8 non-center points and 5 center points, can be evaluated from below equation.

$$N = 2^n + 2n + n_c = 2^2 + 2*2 + 5 = 13 \quad (1)$$

Where N = Total number of experiments needed to be performed, n = Number of independent variables, $n_c$ = Number of centered points.

**Table 4.2:** The experimental range and level of respective independent factors for central composite design.

| Variable | Name | Unit | Low value | High value |
|---|---|---|---|---|
| A (Numeric) | AC | weight percentage | 1 | 5 |
| B (Numeric) | CuCo | weight percentage | 1 | 5 |

### 4.6 Result and discussion

#### 4.6.1 Optimization of ternary composite material based on RSM

13 groups of RSM experiments were produced after the experimental conditions for two influencing factors using design-expert software. The electrochemical performance of ternary PANI/AC/CuCo-based electrode materials was studied. The experimental-specific capacitance results were determined and unified from the CV curve at the scan rate of 1 mV/s in a three-electrode configuration. Table 4.3 displays the final experimental results. Regression analysis used to fit the experimental data yields the second-order polynomial equation, as shown below.

$$C\ (F/g) = 529.81 - 127.38\ A - 66.70\ B - 2.2\ AB + 26.06\ A^2 - 121.29\ B^2 \quad (2)$$

**Table 4.3:** The experimental data and response values obtained by central composite design.

| Sample | Polyaniline (PANI) (Fixed weight percent) | Activated Carbon (AC) (Weight percent) | Copper cobaltite (CuCo) (Weight percent) | Specific Capacitance (F/g) |
|---|---|---|---|---|
| 1 | 4 | 3 | 3 | 523.5 |
| 2 | 4 | 1 | 3 | 695.3 |
| 3 | 4 | 5 | 5 | 248.7 |
| 4 | 4 | 3 | 3 | 529.6 |
| 5 | 4 | 3 | 3 | 533.4 |
| 6 | 4 | 5 | 1 | 372.6 |
| 7 | 4 | 1 | 1 | 613.5 |
| 8 | 4 | 5 | 3 | 421.6 |
| 9 | 4 | 1 | 5 | 498.4 |
| 10 | 4 | 3 | 3 | 521.5 |
| 11 | 4 | 3 | 3 | 535.9 |
| 12 | 4 | 3 | 5 | 330.5 |
| 13 | 4 | 3 | 1 | 491.8 |

Analysis of variance (ANOVA) was used to determine the significance of the fitted equation, as shown in Table 4.4. The F-test resulted in a high F-value of 223.36, which suggested that the model had adequate significance ($P < 0.0001$) based on the findings of the ANOVA. The probability of getting this "model F-value" incorrectly was less than 0.01%. Typically, the P-value was employed to evaluate the importance of model terms. The related model term was more significant, as evidenced by the lower P-value. A, B, $A^2$, and $B^2$ are significant model

terms in this scenario (their P-values were < 0.05). In other terms, the precise capacitance values were significantly influenced by the two variables.

**Table 4.4:** ANOVA Response surface quadratic model for specific capacitance.

| Source | Sum of Squares | df | Mean Square | F-value | P-value |
|---|---|---|---|---|---|
| Model | 1.660E+05 | 5 | 33202.18 | 223.36 | <0.0001* |
| A-AC | 97359.08 | 1 | 97359.08 | 654.95 | <0.0001 |
| B-CuCo | 26693.34 | 1 | 26693.34 | 179.57 | <0.0001 |
| AB | 19.36 | 1 | 19.36 | 0.1302 | 0.7288 |
| $A^2$ | 1876.22 | 1 | 1876.22 | 12.62 | <0.0093 |
| $B^2$ | 40628.57 | 1 | 40628.57 | 273.32 | <0.0001 |
| Residual | 1040.55 | 7 | 148.65 | | |
| Cor Total | 1.671E+05 | 12 | | | |

$R^2$ = 0.9938, $R^2$(Adjusted) = 0.9893, $R^2$(Predicted) = 0.9454

*Significant

The predicted $R^2$ of 0.9454 is in reasonable agreement with the adjusted $R^2$ of 0.9893; i.e. the difference is less than 0.2.

The findings revealed that $R^2$ and adjusted $R^2$ (adjusted) were 0.9938 and 0.9893, respectively. The modified $R^2$ value measures the change in the model's average value, and the value of $R^2$ indicates how effectively the model can predict the experimental datasets. The model is highly relevant as a result. The $R^2$ (predicted) was 0.9454, with a difference of < 0.2 between it and the $R^2$ value. The experimental data of the specific capacitance from the three electrode CV curve fitted the model's anticipated value quite well.

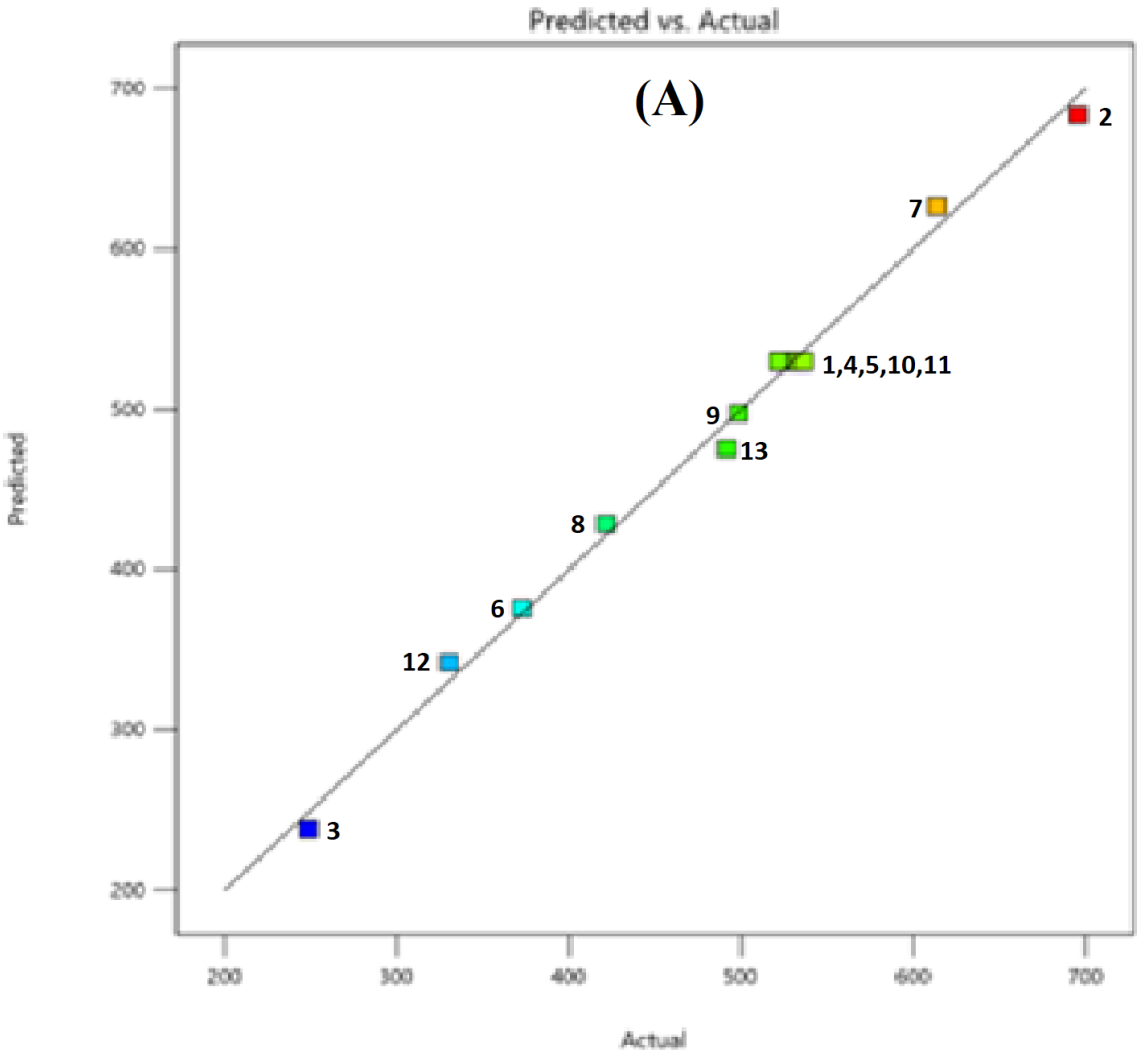
Predicted vs. Actual
(A)
Predicted
Actual
700
600
500
400
300
200
200
300
400
500
600
700
2
7
1,4,5,10,11
9
13
8
6
12
3

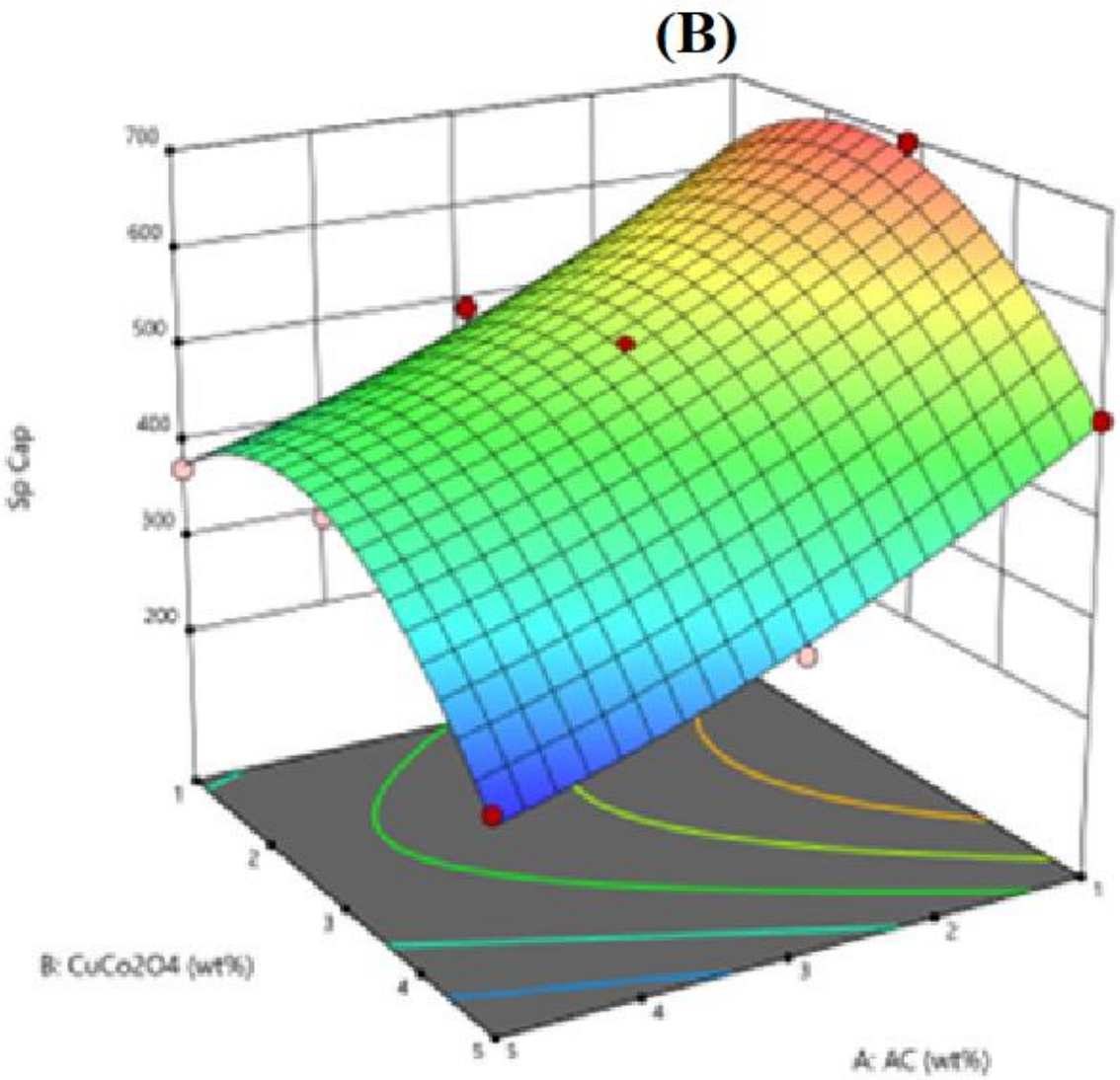
(B)
Sp Cap
700
600
500
400
300
200
B: CuCo2O4 (wt%)
1
2
3
4
5
A: AC (wt%)
1
2
3
4
5

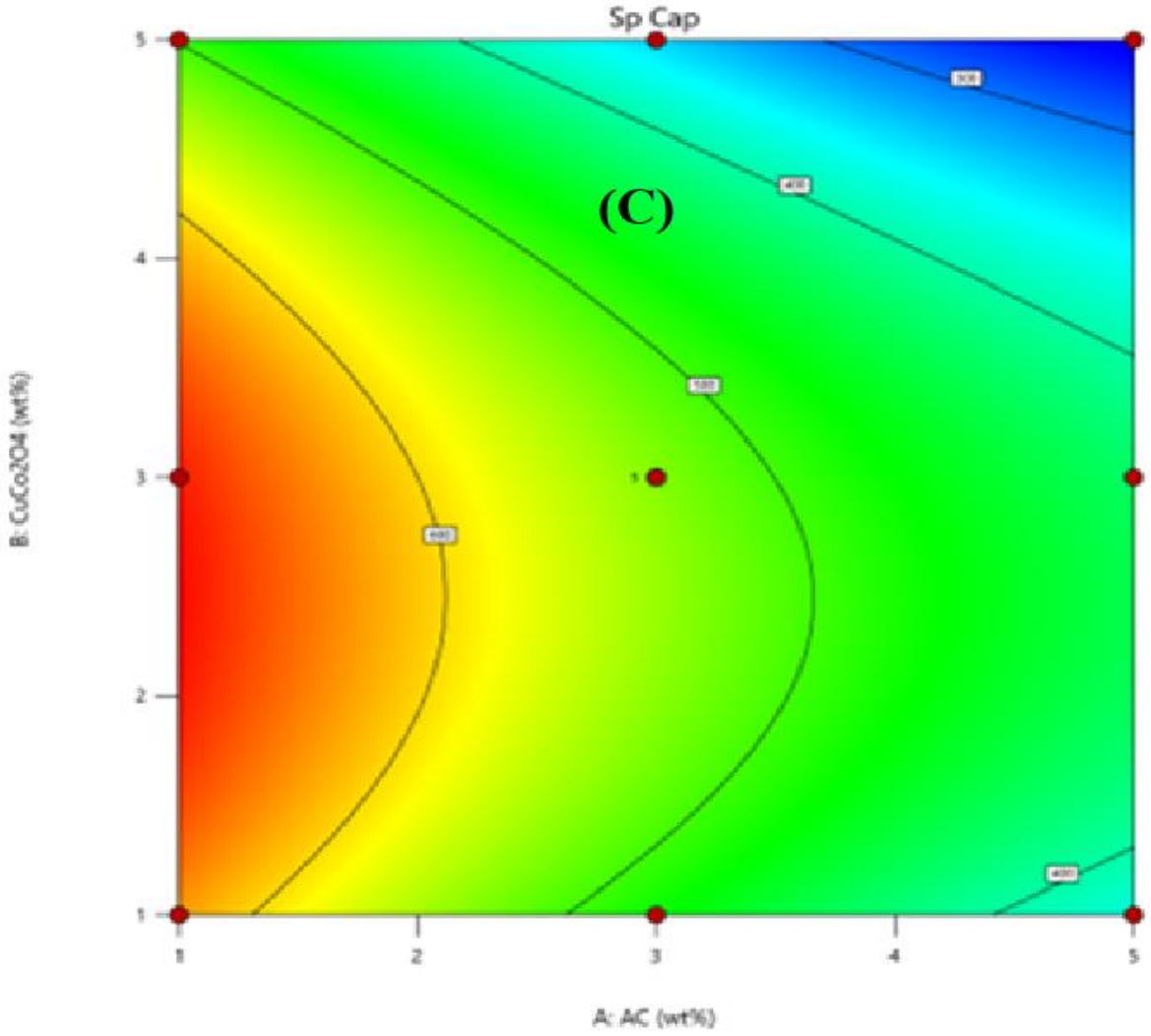


**Fig. 4.13:** (A) Predicted vs. actual response, (B) 3D response surface curve, and (C) contour plot for AC (weight percentage) vs. CuCo (weight percentage)

The primary function and relationship of independent variables can both be studied using the 3D (three-dimensional) response surface map. In order to further analyze the connection and optimum concentrations of the two components in raising specific capacitance, RSM was utilized. The predicted vs. actual response, 3D response surface curve, and contour plot have been displayed in figure 4.13 (A), (B), and (C), respectively. The findings demonstrate that each variable has a maximum value and that the optimization criteria are consistent and obvious. According to the analysis of the response surface method, when the weight ratio of polyaniline, activated carbon, and copper cobaltite in the ternary composite is in the ratio of

4:1:3 (PANI/AC/CuCo), the maximum value of specific capacitance is 683.2 F/g. In summary, three parallel experiments were conducted to verify the model's reliability. The specific capacitance values of 687.7 F/g, 689.2 F/g, and 694.8 F/g were obtained with a mean value of 690.5 F/g, consistent with the predicted value of specific capacitance, showing that the proposed relationship model is highly accurate and reliable.

### 4.6.2 X-ray diffraction

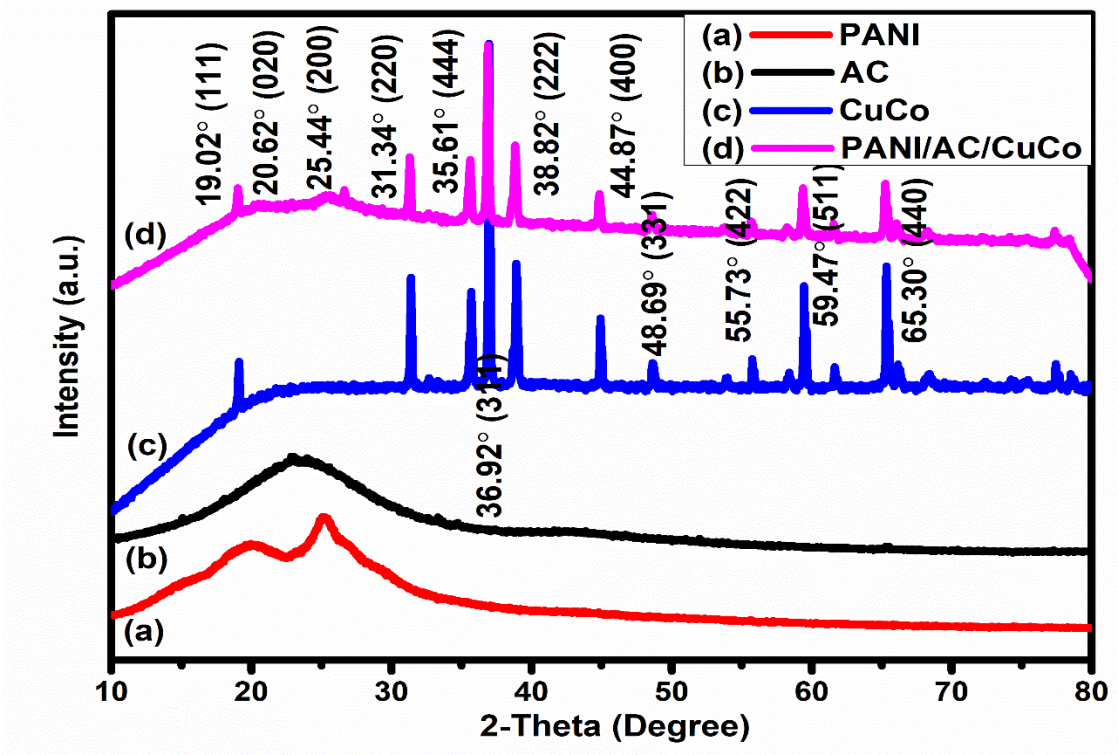


**Fig. 4.14:** XRD patterns of pure PANI, AC, CuCo and optimized ternary composite PANI/AC/CuCo

The XRD patterns of pure PANI, AC, CuCo and optimized ternary composite material PANI/AC/CuCo has been shown in figure 4.14. The characteristic peak pf PANI are clearly visible at 20.01° and 25.2°. A typical carbon based XRD pattern was also observed in pure AC with charatcteristic peak near 23°. Further, the XRD pattern of pure CuCo exhibits highly crystalline behaviour with distinct and sharp peaks. The characteristic diffraction peaks at

20.62° and 25.44° confirm the presence of polyaniline in ternary composite. The peaks at 19.02° (111), 31.34° (220), 35.61° (444), 36.92° (311), 38.82° (222), 44.87° (400), 48.69° (331), 55.73° (422), 59.47° (511), 65.30° (440), and 77.38° (622) indicate the presence of copper cobaltite in the ternary composite material.

### 4.6.3 FTIR

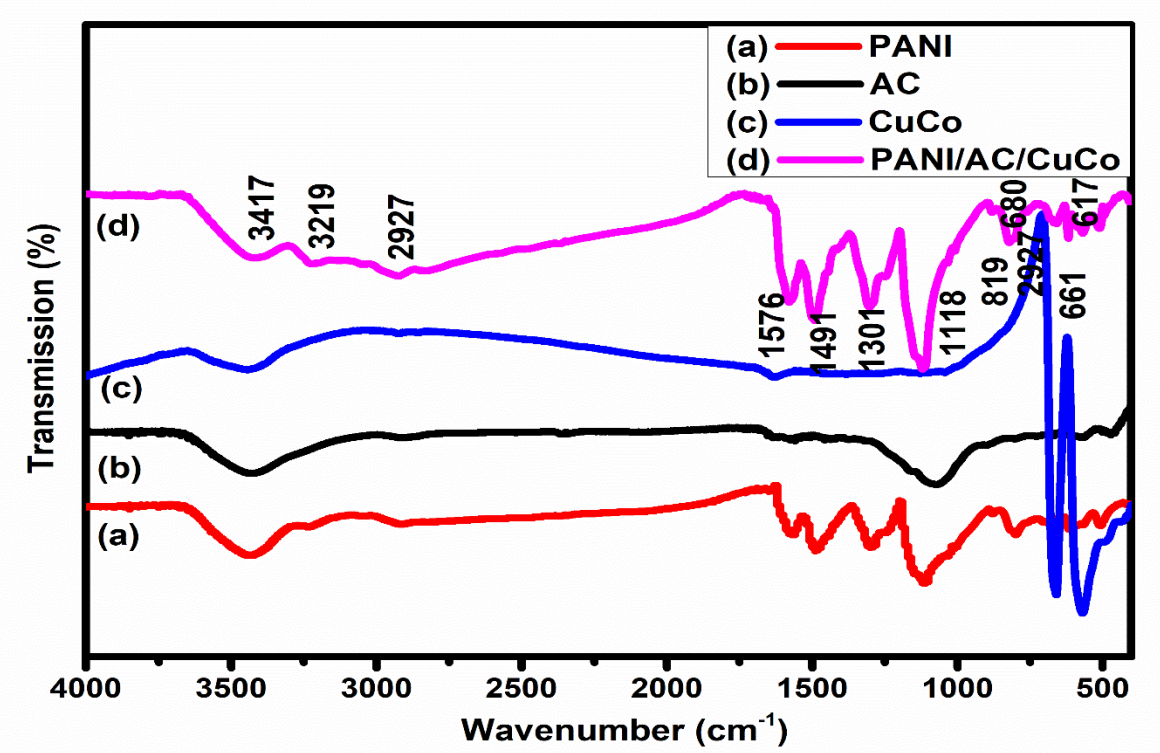


**Fig. 4.15:** FTIR spectra of pure PANI, AC, CuCo and optimized ternary composite PANI/AC/CuCo

The FTIR patterns of pure PANI, AC, CuCo and optimized ternary composite material has been shown in the figure 4.15. The pure PANI and AC exhibited their well defined nature of absorption bands. For, pure CuCo, two sharp and distinct transmission bands are observed which confirm the presence of CuO and CoO. In the case of ternary composite, the absorption bands at 3417 $cm^{-1}$ and 3219 $cm^{-1}$ wavenumbers correspond to $-NH^{2+}$ and -OH stretching vibrations. The band at 2927 $cm^{-1}$ was attributed to -NH bending. Further, the vibrations at

1576 $cm^{-1}$ and 1491 $cm^{-1}$ were present due to C=C stretching vibrations in the quinoid and benzoid rings, respectively. The peak intensity of benzoid form was greater than that of quinoid form of PANI as observed earlier. The -CN shuddering vibrations in the quinoid rings was associated with the absorption band at 1301 $cm^{-1}$. The p-substituted N=Q=N vibrations was referred to as the peak at 1118 $cm^{-1,}$ and -CH deformations due to the presence of PTSA in PANI was attributed to 819 $cm^{-1}$ wavenumber. The -SO stretching due to the presence of PANI was marked at 617 $cm^{-1}$. Further, the absorption bands at 680 $cm^{-1}$ and 561 $cm^{-1}$ were present due to CuO and CoO functional groups in the ternary composite material.

### 4.6.4 Morphological analysis

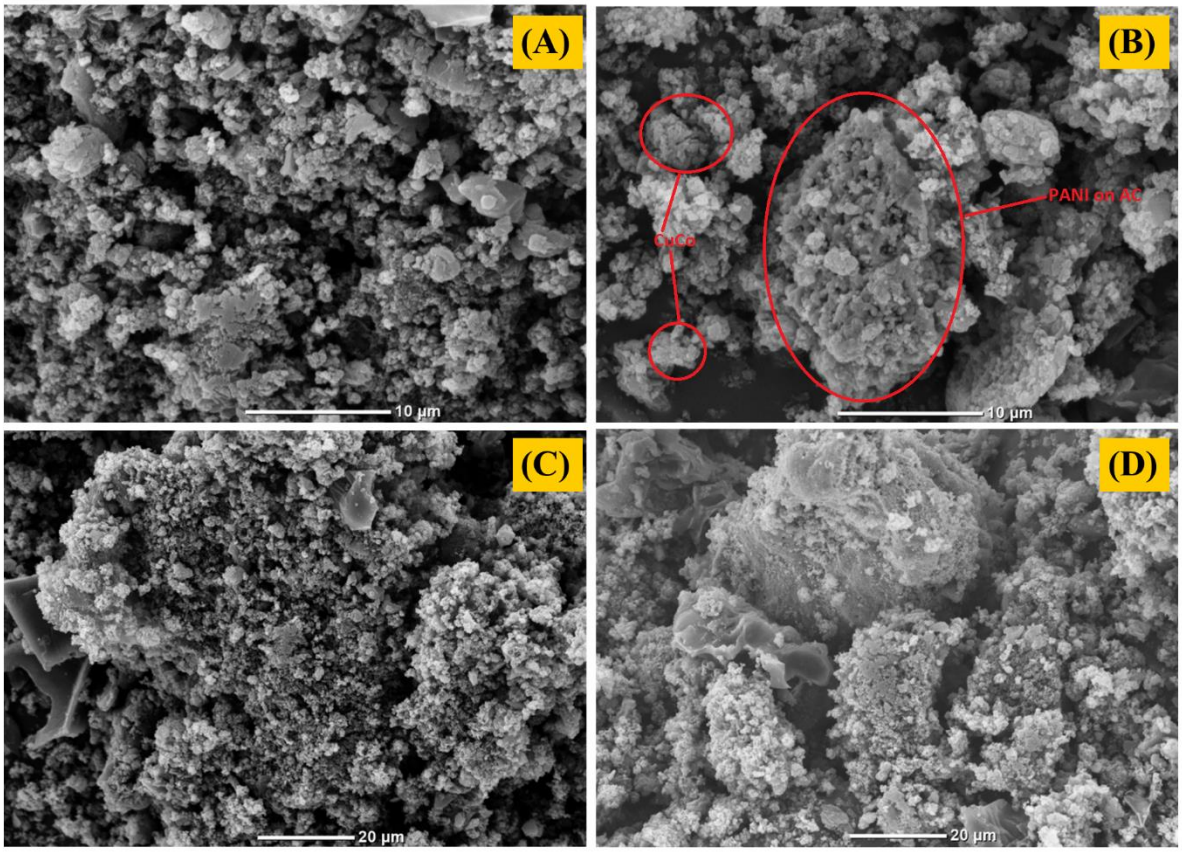


**Fig. 4.16**: SEM micrographs of the optimized ternary composite PANI/AC/CuCo

The SEM micrographs of the optimized ternary composite PANI/AC/CuCo has been provided in figure 4.16. Micelle-like interconnected textures could be observed in the SEM images as

described earlier. The large particles visible in figure 4.16 (B) and (D) are the porous activated carbon. In the other regions, it could be seen that the polyaniline may have covered the activated carbon and copper cobaltite particles.

### 4.6.5 EDX and Elemental Mapping:

The EDX spectrum of the optimized ternary composite PANI/AC/CuCo has been provided in Fig. 4.17. The spectrum clearly shows the presence of all the expected elements. The elemental mapping of the ternary composite material has been given in figure 4.18 (combined and individual), indicating the uniform presence of all the expected elements.

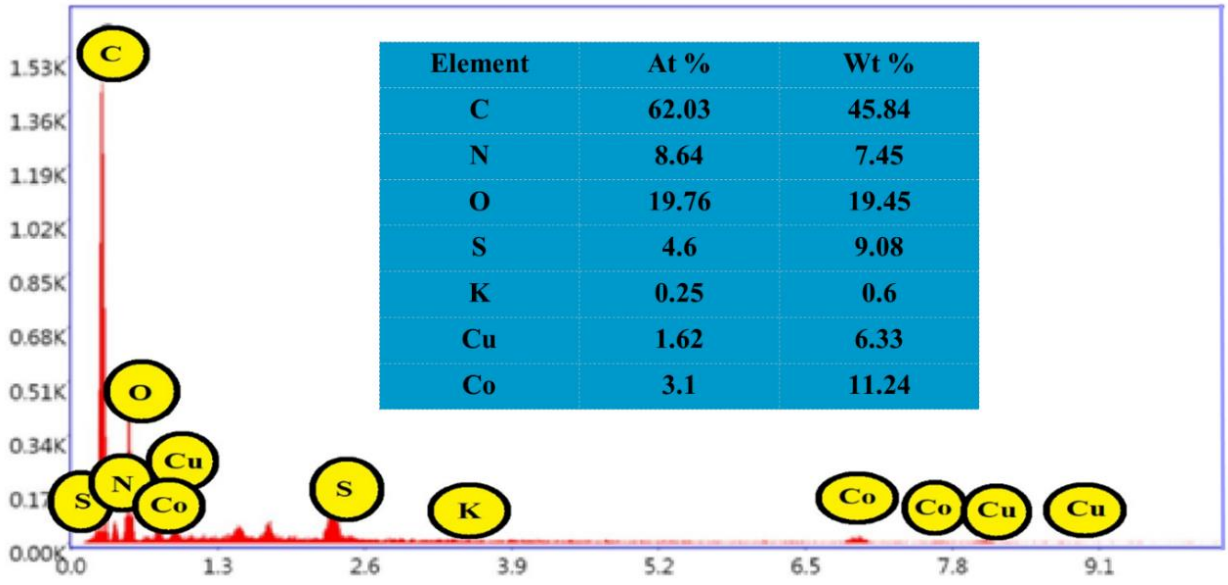


| Element | At % | Wt % |
|---|---|---|
| C | 62.03 | 45.84 |
| N | 8.64 | 7.45 |
| O | 19.76 | 19.45 |
| S | 4.6 | 9.08 |
| K | 0.25 | 0.6 |
| Cu | 1.62 | 6.33 |
| Co | 3.1 | 11.24 |

**Fig. 4.17:** EDX analysis of the optimized ternary composite PANI/AC/CuCo

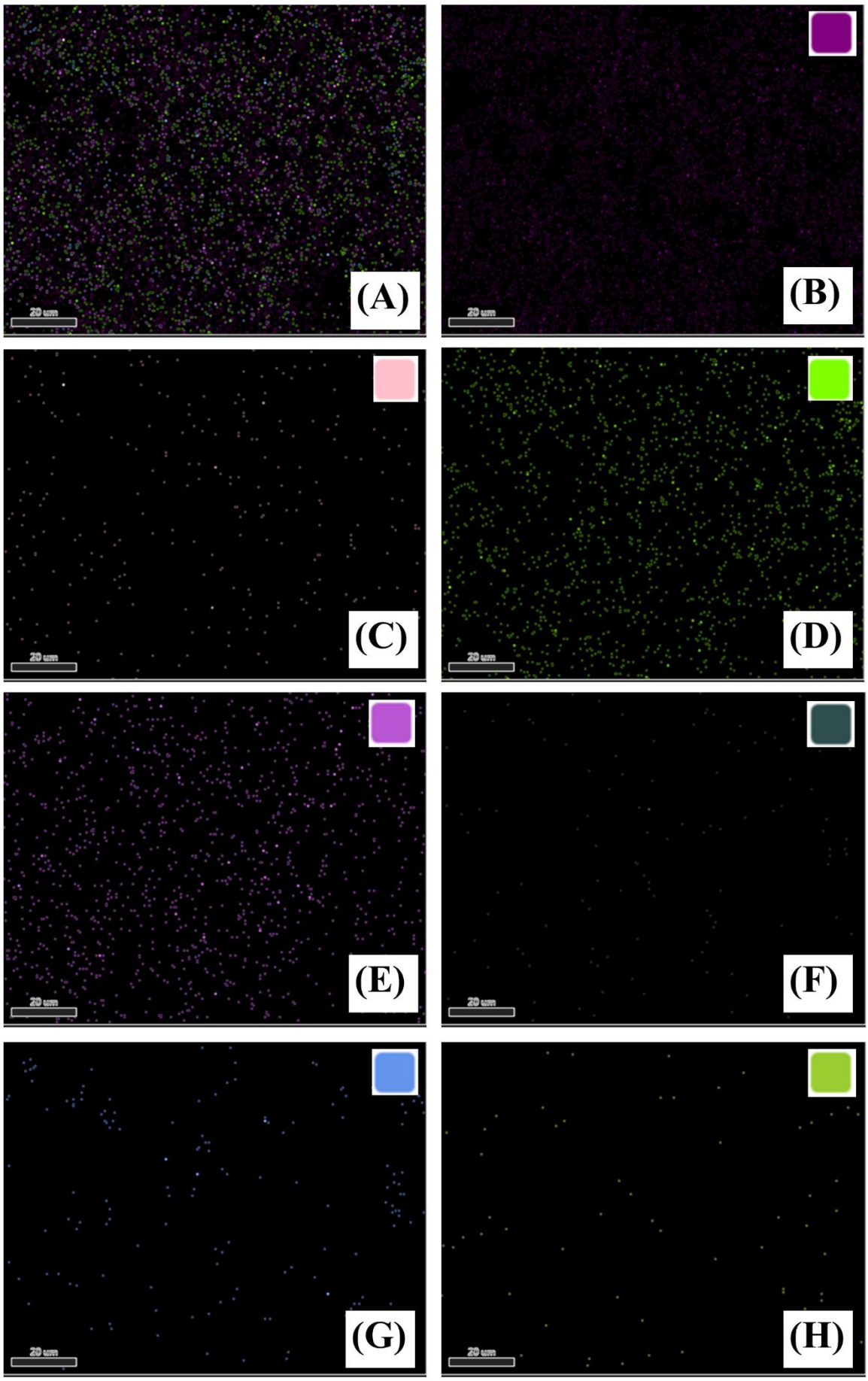
(A)
(B)
(C)
(D)
(E)
(F)
(G)
(H)

**Fig. 4.18:** Elemental mapping for the optimized ternary composite PANI/AC/CuCo, showing (A) overlay, (B) carbon, (C) nitrogen, (D) oxygen, (E) sulfur, (F) potassium, (G) cobalt, (H) copper

### 4.6.6 Electrochemical characterizations:

Cyclic voltammetry of the prepared electrode from optimized ternary composite PANI/AC/CuCo was performed in 3-E and 2-E configurations, as shown in figure 4.17.

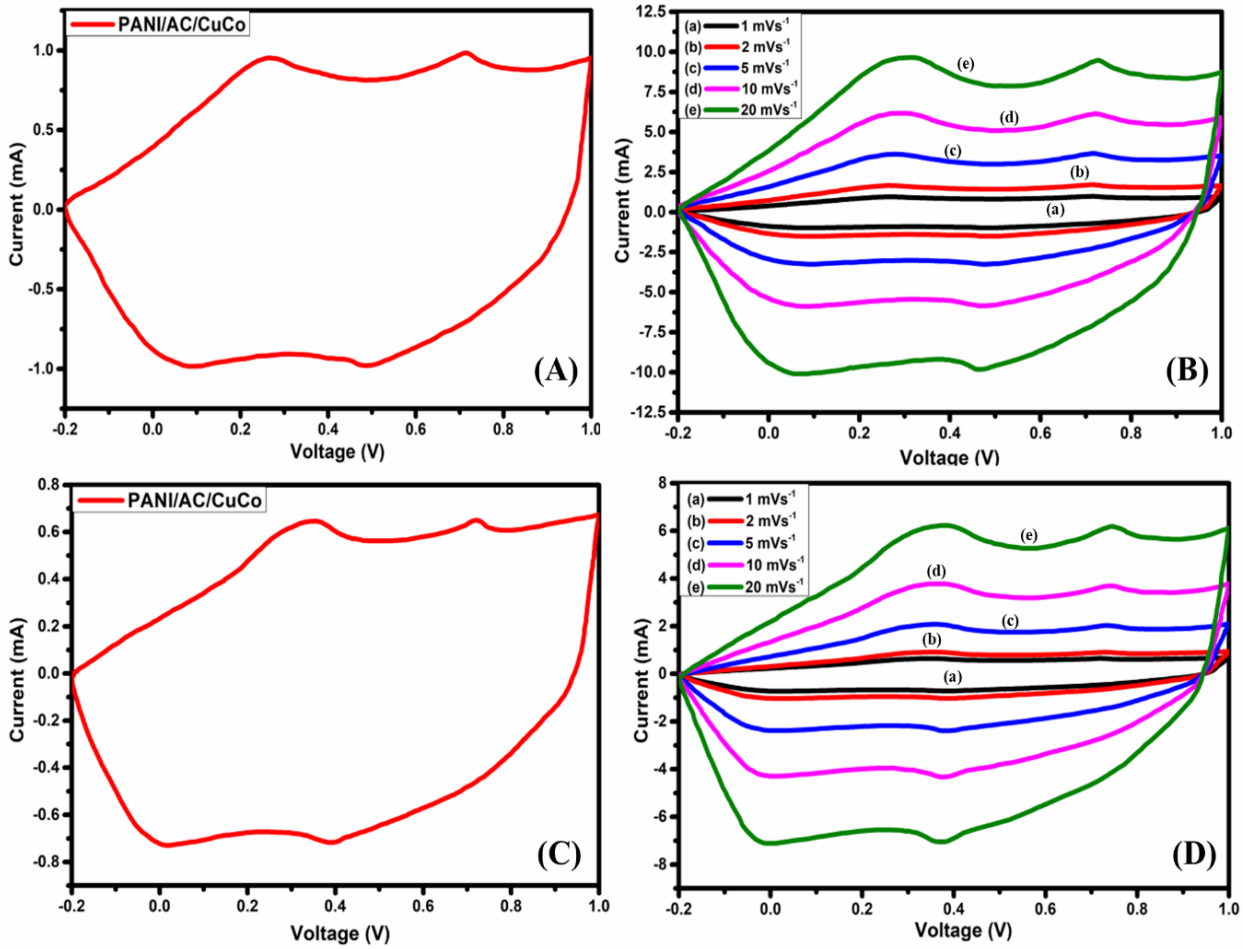


**Fig 4.19:** (A) 3E CV, (B) 3E CV at varying scan rates, (C) 2E CV, (D) 2E CV of ternary at varying scan rates for the optimized ternary composite PANI/AC/CuCo

Figure 4.19 (A) demonstrates the 3-E cyclic voltammogram where peaks in the forward scan were located at 0.27/ 0.71 V, whereas those in the reverse scan were at 0.49/0.08 V,

respectively. The specific capacitance values for PANI/AC/CuCo at 1 $mVs^{-1}$ was 694.8 $Fg^{-1}$. The ternary composite was also tested under varying voltammetric scan rates of 2, 5, 10, and 20 $mVs^{-1}$ (Figure 4.19 (B)). The specific capacitance values for ternary PANI/AC/CuCo at these scan rates were calculated as 568.3, 484.1, 423.4, and 347.7 $Fg^{-1}$. The voltammetric area under the successive curves increases with the scan rate [245], indicating the highly capacitive nature of the optimized ternary material PANI/AC/CuCo. The shifting of the forward scan peaks to the right and that of the reverse scan peaks to the left side indicates strong faradaic and capacitive currents.

The prepared electrodes were also evaluated under a two-electrode symmetric configuration at 1 $mVs^{-1}$ scan rate (Figure 4.19 (C)). The optimized ternary composite PANI/AC/CuCo again demonstrated the highest voltammetric area and highest value of peak current. Further, the voltammetric area under the curves increases with the rise in scan rates to 2, 5, 10, and 20 $mVs^{-1}$ (Figure 4.19 (D)).

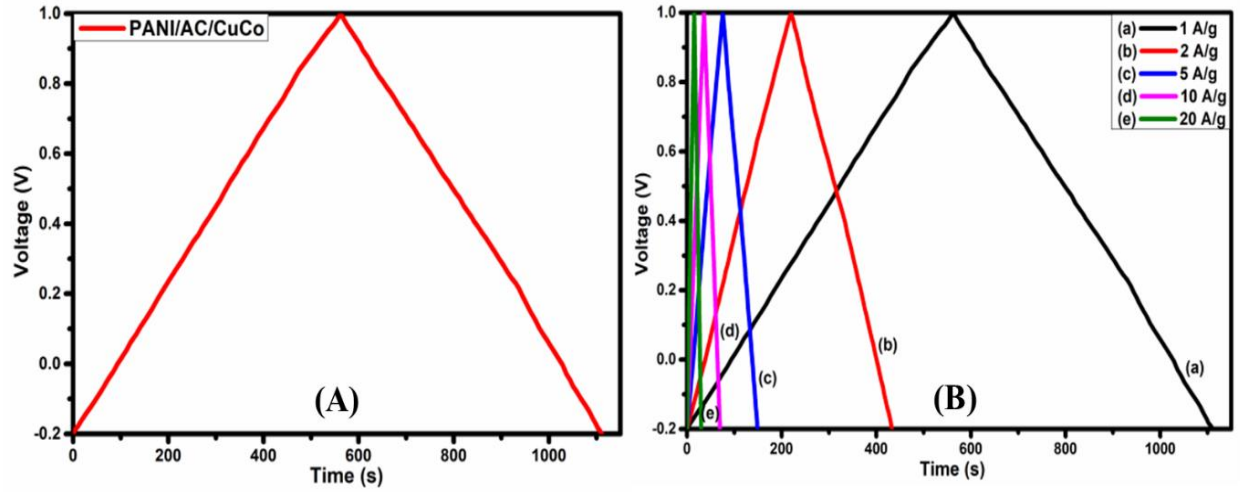


**Fig 4.20:** (A) 2E galvanostatic charge-discharge (B) 2E galvanostatic charge-discharge at varying current density for the optimized ternary composite PANI/AC/CuCo

The galvanostatic charge-discharge tests were conducted for the optimized composite material-based electrodes under 2-E symmetric configuration. The charge-discharge plot at 1 $Ag^{-1}$

current density is shown in figure 4.20 (A). The material demonstrated a similar triangular behavior on the charge-discharge curve with minor plateaus which are attributed to the dual behavior (EDLC and pseudocapacitive). The optimized ternary composite PANI/AC/CuCo was also evaluated under varying current densities of 2, 5, 10, and 20 $Ag^{-1,}$ as shown in figure 4.20 (B). With the rise in current density values, a sharp decline in the charging-discharging times was observed, which is responsible for lower values specific capacitance values.

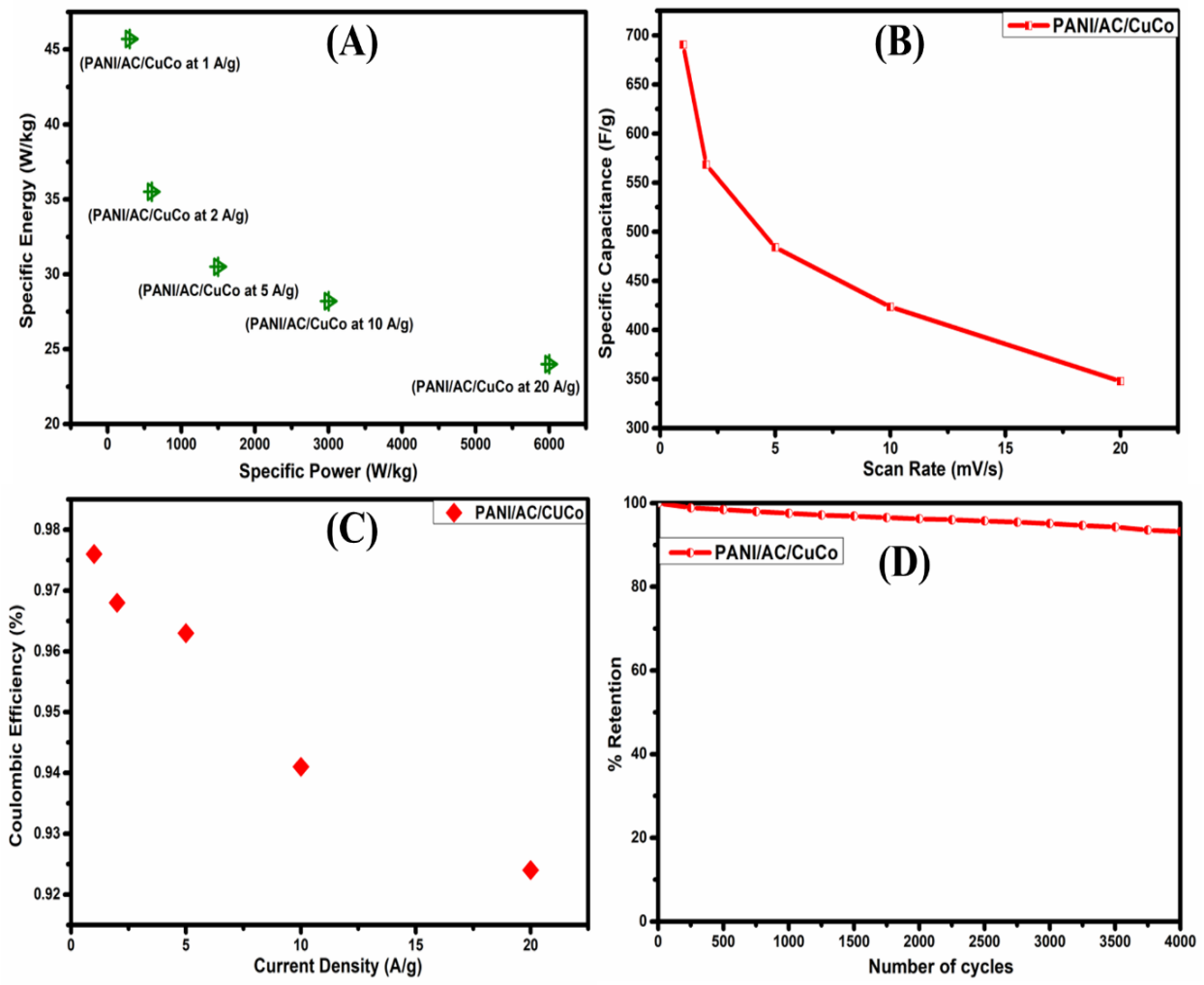


**Fig 4.21:** (A) Ragone plot for the prepared samples, (B) 3E specific capacitance values at different values of voltammetric scan rates, (c) current density vs. coulombic efficiency, (D) Capacitance retention curve

Figure 4.21 (A) shows the Ragone plot for the optimized ternary composite PANI/AC/CuCo. It was observed that at higher values of current density the specific energy density declines whereas the specific power density increases. The peak specific energy density for the optimized ternary composite PANI/AC/CuCo was 45.7 $Whkg^{-1}$ with 300.03 $Wkg^{-1}$ of specific power density. The same ternary composite demonstrated the highest specific power density of 5998.7 W $kg^{-1}$ with a specific energy density of 24.0 $Whkg^{-1}$ at 20 A/g. These high values of specific energy-density and specific power density correspond to the presence of both EDLC and pseudocapacitive type of materials in single composite material. Figure 4.21 (B) demonstrates the variation of measured values of 3- E specific capacitance with scan rate. Figure 4.21 (C), shows the variation of coulombic efficiency with current density, which decreases as current density increases. The capacitance retention tests for the 2E symmetric system were conducted to study the cyclic stability of the fabricated electrodes at a scan rate of 100 mV/s for 4000 cycles. The optimized ternary composite material PANI/AC/CuCo showed outstanding capacitance retention of 93.19 % of the initial value (Figure 4.21 (D)). Table 4.5 shows the different values of specific capacitance, specific energy-density, and specific power-density for the optimized ternary material PANI/AC/CuCo.

**Table 4.5:** The values of specific capacitance ($C_{SP}$), specific energy-density ($E_{SP}$), and specific power-density ($P_{SP}$) for the optimized ternary composite PANI/AC/CuCo.

| **Material** | **Scan Rate (mV/s)** | **$C_{SP}$ (CV 3-E)** | **Current Density (A/g)** | **Esp (Wh/kg)** | **Psp (W/kg)** |
|---|---|---|---|---|---|
| PANI/AC/CuCo | 1 | 694.8 | 1 | 45.7 | 300.0 |
| PANI/AC/CuCo | 2 | 568.3 | 2 | 35.5 | 599.4 |
| PANI/AC/CuCo | 5 | 484.1 | 5 | 30.5 | 1501.1 |

| | | | | | |
|---|---|---|---|---|---|
| PANI/AC/CuCo | 10 | 423.4 | 10 | 28.2 | 3003.2 |
| PANI/AC/CuCo | 20 | 347.7 | 20 | 24.0 | 5998.7 |

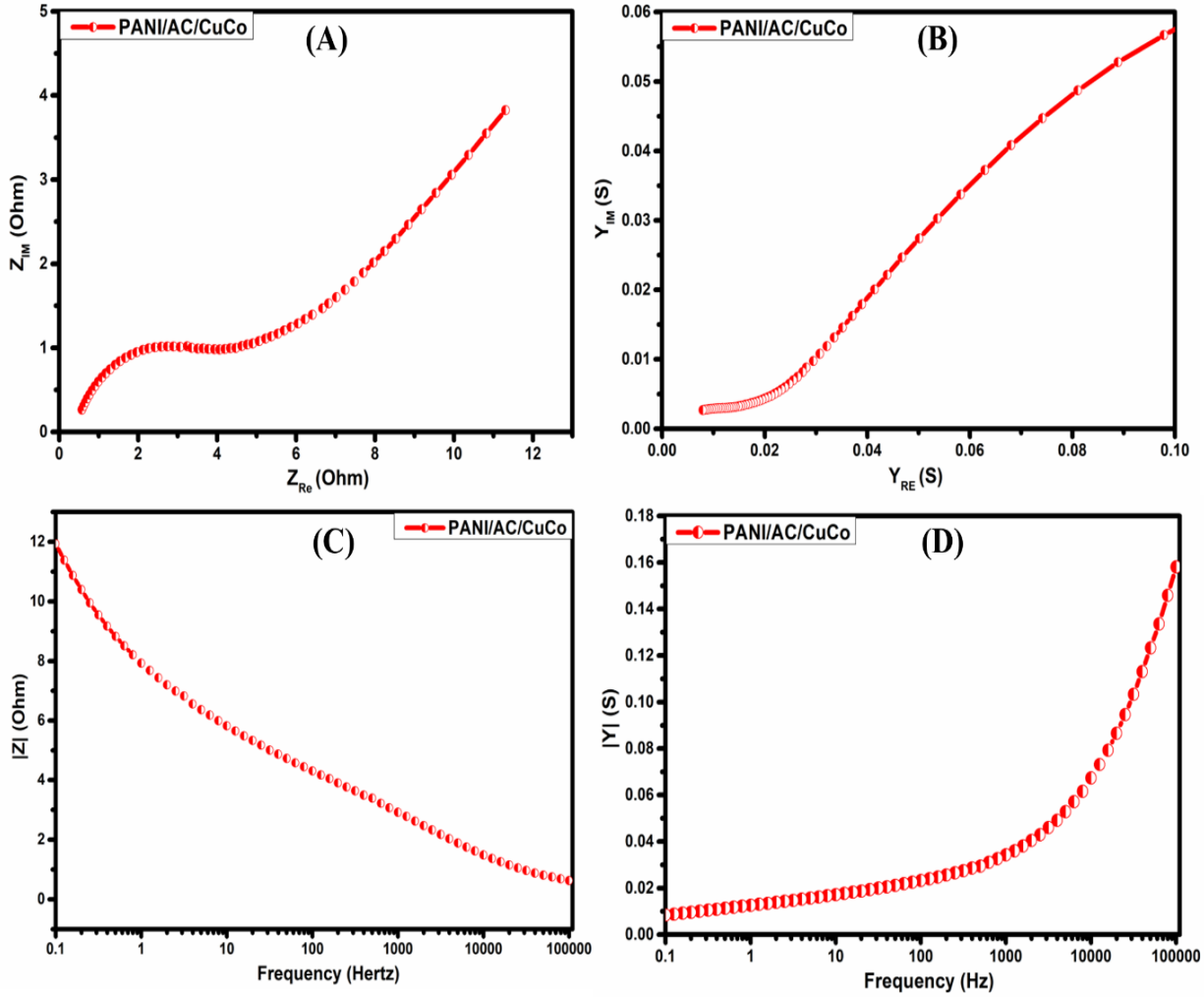


**Fig 4.22:** (A) Electrochemical impedance spectra (EIS) in the complex plane (B) Admittance plots in the complex plane. (C) normalized impedance |Z| vs. freq, (D) normalized admittance |Y| vs. frequency

In order to study the impedance characteristics of the fabricated electrodes from optimized PANI/AC/CuCo, EIS tests were conducted in the frequency range of 0.1 to 100000 Hz. The values of ESR (equivalent series resistance) and Rct (charge transfer resistance) were calculated as 0.9 Ω and 3.9 Ω, respectively, as shown in figure 4.22 (A). Further, the admittance

properties of the fabricated electrodes were also studied in the form of $Y_{RE}$ vs. $Y_{IM}$ plots. Figure 4.22 (B) shows the variation of real admittance ($Y_{RE}$) vs. the imaginary admittance ($Y_{IM}$) for the fabricated electrode from optimized PANI/AC/CuCo. Fig 4.22 (C) shows the variation impedance |Z| with frequency. It was noticed that |Z| decreases with a rise in frequency. Fig 4.22 (D) shows the variation of |Y| vs. frequency. It was observed that with the rise in frequency |Y| increases as electrolyte ions vibrate faster at higher frequencies as opposed to |Z|.

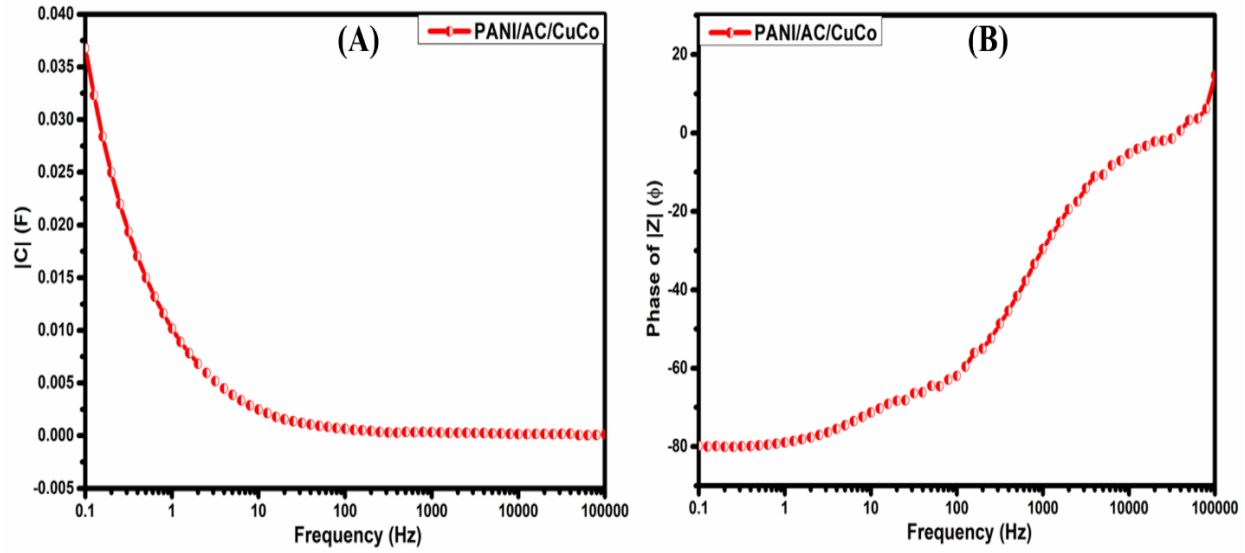


**Fig 4.23:** (A) normalized capacitance |C| vs. frequency, and (B) phase of |Z| (ϕ) vs. frequency

Figure 4.23 (A) manifests the change of capacitance |C| with frequency. The value of total or normalized capacitance decreases with a rise in frequency, which is in good agreement with the EIS results. Figure 4.23 (B) shows the variation of the phase of Z (ϕ) with frequency for the optimized PANI/AC/CuCo. The phase angle in the low-frequency regime is about 80°, indicating its highly pseudocapacitive nature.

### 4.7 Conclusion:

In the current research, the composite material based on polyaniline, activated carbon, and copper cobaltite (PANI/AC/CuCo) has been optimized based on varying weight ratios of AC and CuCo with the help of Response Surface Methodology (RSM). The composite material

with the proportion of 4:1:3 weight ratio of polyaniline, activated carbon, and copper cobaltite shows excellent specific capacitance of 694.8 F/g in a three-electrode configuration. The optimized ternary composite material demonstrated the highest specific energy density of 45.7 Wh/kg and specific power of 5998.7 W/kg. It offers a reasonably high capacitance retention of 93.19 % after the completion of 4000 cycles. The charge transfer resistance of the optimized ternary composite material PANI/AC/CuCo was 1.3 Ω. Based on the above discussions, it can be concluded that on the basis of specific capacitance values, the optimized ternary composite material with a weight ratio of 4:1:3 (PANI: AC: CuCo) was found to be the best material.